J. Fluid Mech. (2021), *vol*. 911, A28, doi:10.1017/jfm.2020.1046

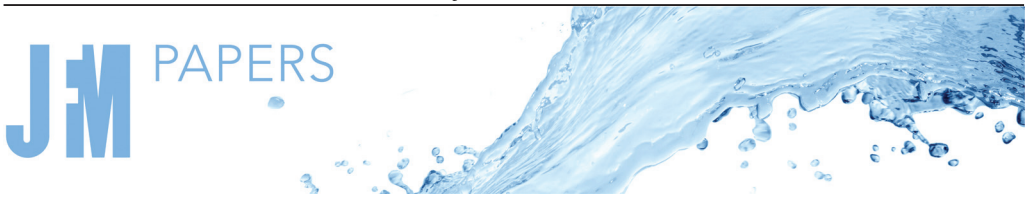

On the streaming in a microfluidic Kundt's tube

Alen Pavlic[1],† **and Jürg Dual**[1]

[1]Institute for Mechanical Systems, ETH Zurich, Tannenstrasse 3, 8092 Zurich, Switzerland

(Received 20 May 2020; revised 30 September 2020; accepted 17 November 2020)

We derive an analytical solution for the acoustic streaming inside a rigid tube resulting from a pseudo-standing wave field, generated by two counterpropagating travelling waves. We solve the second-order axisymmetric problem that follows from the perturbation expansion of the governing equations. In the process, we impose no restriction on the diameter of the tube with respect to the thickness of the viscous boundary layer and acoustic wavelength. The derived solution is then used to study the evolution of streaming patterns inside the tube when geometrical and material parameters are varied. We show how the Schlichting streaming torus at the wall bounds the Rayleigh streaming near the axis of the tube. Decreasing the ratio (Ξ) of the tube radius to the viscous boundary layer thickness gradually expands the Schlichting streaming, suppressing the Rayleigh streaming. Considering the average mass transport velocity, the Rayleigh streaming vanishes at the critical ratio $\Xi_S^M = 6.2$. The critical ratio is independent of fluid properties in the limit of large acoustic wavelength relative to the radius of the tube (Λ). When Λ decreases towards unity, large-scale Eckart-like streaming develops near the axis, superseding the Rayleigh streaming, while the Schlichting streaming remains at the wall. In addition, we demonstrate the relevance of the compressibility of the streaming flow and of the full inclusion of the spatial variation of the Reynolds stress that acts as the streaming source. The study is especially relevant for microfluidic systems, wherein the viscous boundary layer can reach significant thicknesses.

Key words: microfluidics

1. Introduction

Kundt's tube is arguably one of the best-known experimental devices in acoustics, nowadays used worldwide in the physics educational curriculum (Jaafar *et al.* 2016; Papacosta & Linscheid 2016; Bates 2017). It was proposed by August Kundt (1866) to measure the speed of sound in fluids. The fluid in the tube contains small particles (e.g.

† Email address for correspondence: apavlic@ethz.ch

cork dust) and is periodically excited either via rubbing of the metal rod resonator at one end of the tube (Kundt 1866), or by means of an electrically-driven tuning fork (Cook 1926) or a vibrating diaphragm (Andrade 1931). The distance between the groups of particles that, over time, gather at the nodes of vibration is then measured. This distance corresponds to one-half of the acoustic wavelength λ. The latter leads to the speed of sound c_f through the expression $c_f = \lambda f$, with a known excitation frequency f. This visually appealing motion of particles attracted many experimentalists, especially in the time between the introduction of Kundt's tube in 1866 and the middle of the 20th century. Their investigations revolved mainly around the visual inspection of figures formed by particles inside the tube (Dvorak 1874, 1876; Cook 1926, 1930*a*,*b*, 1931; Irons 1929*a*,*b*; Andrade 1931, 1932; Hutchisson & Morgan 1931; Schuster & Matz 1940). At the start of the 21st century, physically similar phenomena emerged in the context of microfluidic devices for manipulation of cells and particles with ultrasonic waves. Sobanski *et al.* (2000) used standing waves in the radial direction of the capillary with a circular cross-section for the detection of sub-micron particles. Standing waves along the axis of the capillary were used by Wiklund, Nilsson & Hertz (2001) for size-selective trapping and subsequent separation of micrometre-sized particles. Araz, Lee & Lal (2003) introduced a method for manipulation of micrometre-sized particles in a capillary excited in a bending mode. Particle-focusing within a capillary with a constant backflow was demonstrated by Goddard *et al.* (2006), for use in a flow cytometer. More recently, Gralinski *et al.* (2014) used ultrasonic standing waves along the axis of a glass capillary to trap and concentrate particles, preparing them for multiaxial optical analysis and for other batch operations.

In such systems, the movement of particles is dictated by many forces, namely inertia, the viscous drag from fluid flow, hydrodynamic interactions, contact forces and acoustic radiation forces. One of the underlying physical phenomena is acoustic streaming, which can be described as a steady circulatory flow in a periodically excited fluid. Streaming can be dominant for particles smaller than a critical radius, thereby disturbing trapping in acoustofluidic applications.

In a Kundt's tube, this phenomenon was first reported by Dvorak (1876). He observed that air flows from a velocity node towards the antinode along the axis of the tube, while the flow of air near the wall is directed in the opposite direction. Andrade (1931) confirmed the flow direction observed by Dvorak (1876) using improved experimental techniques, the main improvements being diaphragm excitation driven by an alternating current, and the use of a camera to capture the particle patterns. However, Andrade (1931) argued that the physical principle causing the behaviour of small particles in Dvorak's experiments was not solely the acoustic streaming, but was rather closely related to the formation of an antinodal disc (see Andrade 1932). The latter is a disc-like agglomeration of dust at antinodes of vibration that appears at lower frequencies, most likely due to the acoustic radiation force.

Even though Dvorak's experimental results (Dvorak 1876), on which he based his description of the direction of the streaming, were later questioned by Andrade (1931), Dvorak's conclusions motivated Rayleigh (1884) to develop the first analytical solution for the reported phenomenon. Consequently, the streaming directed from a velocity node towards the antinode in the centre of the channel, and oppositely directed near the wall, is nowadays called the Rayleigh streaming. Rayleigh (1884) assumed the viscous boundary layer thickness to be small and the acoustic wavelength to be large, both relative to the tube diameter. This restricts the applicability of his formulation to low-viscosity fluids and middle-range frequency excitations. Furthermore, for the sake of simplicity, Rayleigh

assumed a two-dimensional geometry extending infinitely in the out-of-plane direction. More than half a century later, Westervelt (1953) and Nyborg (1953) extended Rayleigh's approach to compressible fluid at the first order of perturbation expansion. A different case was considered by Schlichting (1932), who solved the incompressible streaming problem near the wall. The so-called Schlichting streaming is known to appear between the wall and the Rayleigh streaming in the bulk of a fluid. Its direction of rotation is opposite that of the Rayleigh streaming.

The two-dimensional theory was extended by Hamilton, Ilinskii & Zabolotskaya (2003*a*) to a channel of an arbitrary width relative to the viscous boundary layer thickness, extending infinitely in the out-of-plane direction. They showed that the oppositely directed Schlichting streaming vortices, between the Rayleigh vortices and the wall, could become dominant as the thickness of the viscous boundary layer was increased. More recently, Doinikov, Thibault & Marmottant (2017) considered a fluid bounded between an elastic solid wall and a reflector, posing no restrictions on the width of the channel. The standing wave in their case was generated via two counterpropagating leaky waves, originating from the solid wall.

The first to extend Rayleigh's approach to cylindrical geometry were Schuster & Matz (1940). They derived a very concise expression for the streaming velocity and analysed the magnitude of the streaming. (The expression for the streaming velocity by Schuster & Matz (1940) is later used for comparison, and is given explicitly in appendix G.) The latter was found to scale with the square of the pressure amplitude inside the tube, which was confirmed experimentally. The solution of Schuster & Matz (1940), although very convenient, relies on many assumptions: the viscous boundary layer is assumed small compared to the tube radius; the acoustic wavelength is assumed large with respect to the tube radius; the wave is assumed undamped along the tube axis. All of this considerably restricts the applicability of their solution. In more recent years, others have also analysed various aspects of streaming in a tube (Qi, Johnson & Harris 1995; Menguy & Gilbert 2000; Bailliet *et al.* 2001; Hamilton, Ilinskii & Zabolotskaya 2003*b*).

Recently, Baltean-Carlès *et al.* (2019) analysed the contributions of individual parts of the streaming source terms, and how they are affected by the finite length of the tube relative to the diameter. They discovered that the standard exclusion of terms is invalid when the length of the tube becomes comparable to its diameter.

Here, we derive a general analytical solution for the acoustic streaming that results from a pseudo-standing wave field in a tube of an arbitrary diameter. The acoustic field is generated by two counterpropagating decaying travelling waves, which is a common approach for generating acoustic fields in standing surface acoustic wave (SSAW) systems (Devendran *et al.* 2016). We use an approach similar to that of Doinikov *et al.* (2017), but consider a cylindrical geometry and a rigid wall. We also extend the formulation by considering the complete spatial variation of the Reynolds stress as a source term for the streaming, and by considering also the irrotational component of the streaming velocity (i.e. assuming that the streaming flow is compressible). First, we derive the dispersion equation to determine the wavenumber in the fluid. Then we solve the first- and the second-order problems that follow from the perturbation expansion. The solution is valid inside as well as outside the viscous boundary layer, which is of unrestricted thickness. It therefore covers also very thin capillaries, where the viscous boundary layer is comparable to the radius. The solution is then used to analyse the evolution of streaming vortices with respect to changes in the fluid viscosity, tube diameter and excitation frequency. In addition, we analyse the importance of the irrotational part of the streaming velocity and of individual parts of the spatial variation of the Reynolds stress (Lighthill 1978) that acts

as a source term in the streaming equations. Some of those parts are often assumed to be negligible (e.g. Rayleigh 1884; Schlichting 1932; Lighthill 1978; Doinikov *et al.* 2017). The impact of different assumptions on the streaming with respect to the increasing viscous boundary layer thickness relative to the tube diameter is investigated.

2. Problem statement and assumptions

We assume that the fluid, initially at rest, is situated in an infinite rigid tube with an inner diameter of $2a$. The geometry of our problem is parametrized in cylindrical coordinates, as depicted in figure 1, and is symmetric with respect to the z-axis oriented along the centre of the tube. In the fluid, there are two counterpropagating spatially-decaying harmonic travelling waves along the axis of the tube, which form a pseudo-standing wave when superimposed. The acoustic field resembles a standing wave near the plane of symmetry ($z = 0$), approaching a travelling-wave-like behaviour far away from the plane of symmetry. We neglect thermal effects, and the motion of a barotropic compressible viscous fluid is therefore governed by the Navier–Stokes equations

$$\rho\frac{\partial \boldsymbol{v}}{\partial t} + \rho(\boldsymbol{v}\cdot\boldsymbol{\nabla})\boldsymbol{v} = -\boldsymbol{\nabla}p + \eta\nabla^2\boldsymbol{v} + \left(\eta_B + \frac{\eta}{3}\right)\boldsymbol{\nabla}(\boldsymbol{\nabla}\cdot\boldsymbol{v}), \tag{2.1}$$

the continuity equation

$$\frac{\partial \rho}{\partial t} + \boldsymbol{\nabla}\cdot(\rho\boldsymbol{v}) = 0 \tag{2.2}$$

and the equation of state

$$p = p(\rho). \tag{2.3}$$

The three variables in (2.1), (2.2) and (2.3) are the velocity $\boldsymbol{v}$, pressure p and density ρ. The material constants involved are the dynamic and bulk viscosity, η and η_B, respectively. To constrain the problem, the no-slip boundary condition is imposed at the wall.

By applying a regular perturbation technique (Hamilton & Blackstock 1998, p. 281), the problem can be solved in successive steps of increasing order in terms of the small Mach number

$$\varepsilon = \frac{v_a}{c_f} \ll 1, \tag{2.4}$$

with the amplitude of the fluid velocity denoted by v_a, and the speed of sound in the fluid by c_f. The perturbed variables can then be written in the form of a series, namely $\square = \widehat{\square}_0 + \varepsilon\widehat{\square}_1 + \varepsilon^2\widehat{\square}_2 + \cdots$, where the subscript denotes the order in the perturbation expansion. In our formulation, we will use $\square_0 = \widehat{\square}_0$, $\square_1 = \varepsilon\widehat{\square}_1$, $\square_2 = \varepsilon^2\widehat{\square}_2$, and solve the associated first- and second-order problems. Following our assumptions, $\boldsymbol{v}_0 = \boldsymbol{0}$.

3. Fluid motion at the first order

The perturbation expansion of the governing equations to the first order results in the momentum equations

$$\rho_0\frac{\partial \boldsymbol{v}_1}{\partial t} = -\boldsymbol{\nabla}p_1 + \eta\nabla^2\boldsymbol{v}_1 + \left(\eta_B + \frac{\eta}{3}\right)\boldsymbol{\nabla}(\boldsymbol{\nabla}\cdot\boldsymbol{v}_1) \tag{3.1}$$

and the continuity equation

$$\frac{\partial \rho_1}{\partial t} = -\rho_0\boldsymbol{\nabla}\cdot\boldsymbol{v}_1, \tag{3.2}$$

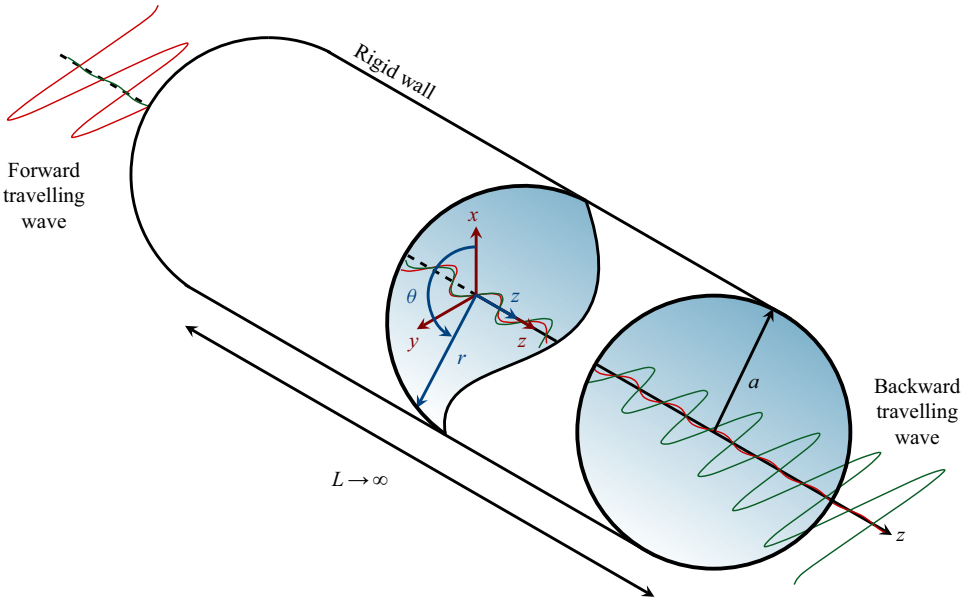

Figure 1. The geometry in a cylindrical coordinate system (r, θ, z) that serves as a basis for the analytical solution. The fluid is bounded within a rigid tube of radius a and of infinite length L.

with equilibrium density ρ_0. The first-order pressure and density are related through the linear equation of state

$$p_1 = c_f^2 \rho_1. \tag{3.3}$$

Using the Helmholtz decomposition

$$\boldsymbol{v}_1 = \boldsymbol{\nabla}\varphi_1 + \boldsymbol{\nabla} \times \boldsymbol{\psi}_1 \tag{3.4}$$

(e.g. Blackstock 2001, p. 76), the first-order velocity field can be separated into a sum of the gradient of a scalar velocity potential φ_1 and the curl of a divergence-free vector velocity potential $\boldsymbol{\psi}_1$. First-order fields are assumed to have a harmonic time-dependence, i.e. $\square_1(\boldsymbol{x}, t) = \mathrm{Re}[\tilde{\square}_1(\boldsymbol{x})\mathrm{e}^{-\mathrm{i}\omega t}]$ with angular frequency ω, where $\mathrm{Re}[\square]$ denotes the real part of $\square$, and $\tilde{\square}_1(\boldsymbol{x})$ is the complex amplitude of the corresponding first-order field $\square_1(\boldsymbol{x}, t)$. Using this assumption and inserting (3.4) in (3.1), (3.2), (3.3) leads to the set of first-order potential equations

$$\nabla^2\varphi_1 + k_f^2\varphi_1 = 0, \tag{3.5}$$

$$\nabla^2\boldsymbol{\psi}_1 + k_v^2\boldsymbol{\psi}_1 = \boldsymbol{0}, \tag{3.6}$$

with the wavenumber in an unbounded viscous fluid

$$k_f = \frac{\omega}{c_f}\left[1 - \frac{\mathrm{i}\omega}{\rho_0 c_f^2}\left(\eta_B + \frac{4}{3}\eta\right)\right]^{-1/2} \tag{3.7}$$

(Blackstock 2001, p. 305), and the viscous wavenumber

$$k_v = \frac{\mathrm{i}+1}{\delta}, \tag{3.8}$$

where δ represents the thickness of the viscous boundary layer and is computed as

$$\delta = \sqrt{\frac{2\eta}{\rho_0 \omega}}. \tag{3.9}$$

We assume that there is a forward and a backward travelling wave inside the fluid, which form a pseudo-standing wave along the z-axis when superimposed. The pseudo-standing wave potentials therefore follow as a sum of potentials of forward and backward travelling waves, namely

$$\varphi_1 = \varphi_1^+ + \varphi_1^-, \tag{3.10}$$

$$\boldsymbol{\psi}_1 = \boldsymbol{\psi}_1^+ + \boldsymbol{\psi}_1^-, \tag{3.11}$$

with superscripts $\square^+$ and $\square^-$ identifying the forward and the backward travelling waves, respectively. Based on the axial symmetry of the problem, we assume the following form of potentials:

$$\varphi_1^+ = F(r)\exp(\mathrm{i}(kz - \omega t)), \tag{3.12}$$

$$\varphi_1^- = F(r)\exp(\mathrm{i}(-kz - \omega t)), \tag{3.13}$$

$$\boldsymbol{\psi}_1^+ = G(r)\exp(\mathrm{i}(kz - \omega t))\boldsymbol{e}_\theta, \tag{3.14}$$

$$\boldsymbol{\psi}_1^- = G(r)\exp(\mathrm{i}(-kz - \omega t))\,(-\boldsymbol{e}_\theta)\,, \tag{3.15}$$

with the basis vector $\boldsymbol{e}_\theta$ of unit length, unknown functions $F(r)$ and $G(r)$, and an unknown complex wavenumber k.

To find the functions $F(r)$ and $G(r)$, we insert the potentials of the forward travelling wave, (3.12) and (3.14), into (3.5) and (3.6), which leads to

$$\left[\frac{\mathrm{d}^2F(r)}{\mathrm{d}r^2} + \frac{1}{r}\frac{\mathrm{d}F(r)}{\mathrm{d}r} + q_f^2 F(r)\right]\exp(\mathrm{i}(kz - \omega t)) = 0 \tag{3.16}$$

and

$$\left[\frac{\mathrm{d}^2G(r)}{\mathrm{d}r^2} + \frac{1}{r}\frac{\mathrm{d}G(r)}{\mathrm{d}r} + \left(q_v^2 - \frac{1}{r^2}\right)G(r)\right]\exp(\mathrm{i}(kz - \omega t)) = 0, \tag{3.17}$$

with

$$q_f^2 = k_f^2 - k^2, \tag{3.18}$$

$$q_v^2 = k_v^2 - k^2. \tag{3.19}$$

The unknown functions $F(r)$ and $G(r)$ are the solutions to the Sturm–Liouville equations that follow from the r-dependent part of (3.16) and (3.17), and can be expressed as

$$F(r) = A_1 J_0(q_f r) + A_2 Y_0(q_f r), \tag{3.20}$$

$$G(r) = B_1 J_1(q_v r) + B_2 Y_1(q_v r), \tag{3.21}$$

with constants A_1, A_2, B_1, B_2, and nth-order Bessel functions J_n and Y_n of the first and of the second kind, respectively. Because the velocity has to be finite at $r = 0$, A_2 and B_2 have to be zero, which yields

$$F(r) = A_1 J_0(q_f r), \tag{3.22}$$

$$G(r) = B_1 J_1(q_v r). \tag{3.23}$$

3.1. *Dispersion relation and the unknown constants at the first order*

The first-order velocity field of a forward travelling wave can be written in a potential form as

$$\boldsymbol{v}_1^+ = \boldsymbol{\nabla}\varphi_1^+ + \boldsymbol{\nabla}\times\boldsymbol{\psi}_1^+. \tag{3.24}$$

We substitute (3.12) and (3.14) into (3.24), which leads to the velocity field of a forward travelling wave,

$$\boldsymbol{v}_1^+ = \left[\left(\frac{\mathrm{d}F(r)}{\mathrm{d}r} - \mathrm{i}kG(r)\right)\boldsymbol{e}_r + \left(\mathrm{i}kF(r) + \frac{1}{r}G(r) + \frac{\mathrm{d}G(r)}{\mathrm{d}r}\right)\boldsymbol{e}_z\right]\exp(\mathrm{i}(kz-\omega t)), \tag{3.25}$$

with basis vectors $\boldsymbol{e}_r$ and $\boldsymbol{e}_z$ of the cylindrical coordinate system. In order to find the dispersion relation and the unknown constants A_1 and B_1, we apply the no-slip boundary condition to the fluid at the wall of the tube, namely

$$\boldsymbol{v}_1^+\big|_{r=a} = \boldsymbol{0}, \tag{3.26}$$

where $\square|_{r=a}$ denotes the evaluation of $\square$ at $r=a$. Substituting the solutions (3.22) and (3.23) into (3.25) and using the condition (3.26) leads to a system of two equations,

$$\left[-q_f J_1(q_f a)\right]A_1 + \left[-\mathrm{i}kJ_1(q_v a)\right]B_1 = 0, \tag{3.27}$$

$$\left[\mathrm{i}kJ_0(q_f a)\right]A_1 + \left[q_v J_0(q_v a)\right]B_1 = 0. \tag{3.28}$$

The system of (3.27) and (3.28) has a non-trivial solution only if the determinant of the system equals zero, i.e.

$$\begin{vmatrix} -q_f J_1(q_f a) & -\mathrm{i}kJ_1(q_v a) \\ \mathrm{i}kJ_0(q_f a) & q_v J_0(q_v a) \end{vmatrix} = 0. \tag{3.29}$$

This leads to the dispersion relation

$$K(k_R, k_I) = q_f q_v J_0(q_v a)J_1(q_f a) + k^2 J_0(q_f a)J_1(q_v a) = 0, \tag{3.30}$$

which is used to numerically find the real and the imaginary parts of the wavenumber k, defined as $k_R = \mathrm{Re}[k]$ and $k_I = \mathrm{Im}[k]$, respectively. The equations leading to both parts of the wavenumber are

$$\mathrm{Re}\left[K(k_R, k_I)\right] = 0, \tag{3.31}$$

$$\mathrm{Im}\left[K(k_R, k_I)\right] = 0. \tag{3.32}$$

The wavenumber is later calculated for water, oil, glycerol and air (see § 5 and appendix A).

We can now use one of the equations, e.g. (3.27), and express one of the unknown constants in terms of the second, which is a fitting parameter determined by the pressure profile of the wave. In our case, we choose A_1 as a fitting parameter, and B_1 then follows as

$$B_1 = \mathrm{i}\frac{q_f J_1(q_f a)}{kJ_1(q_v a)}A_1. \tag{3.33}$$

3.2. *First-order velocity field*

The velocity field of the backward travelling wave is obtained by substituting (3.13) and (3.15) into (3.4):

$$\boldsymbol{v}_1^- = \left[\left(\frac{\mathrm{d}F(r)}{\mathrm{d}r} - \mathrm{i}kG(r)\right)\boldsymbol{e}_r + \left(-\mathrm{i}kF(r) - \frac{1}{r}G(r) - \frac{\mathrm{d}G(r)}{\mathrm{d}r}\right)\boldsymbol{e}_z\right]\exp(\mathrm{i}(-kz-\omega t)). \tag{3.34}$$

The total velocity field is then obtained by summing (3.25) and (3.34):

$$\begin{aligned}\boldsymbol{v}_1 = \Bigg[&\left(\frac{\mathrm{d}F(r)}{\mathrm{d}r} - \mathrm{i}kG(r)\right)2\cos(kz)\boldsymbol{e}_r \\ &+ \left(\mathrm{i}kF(r) + \frac{1}{r}G(r) + \frac{\mathrm{d}G(r)}{\mathrm{d}r}\right)2\mathrm{i}\sin(kz)\boldsymbol{e}_z\Bigg]\exp(-\mathrm{i}\omega t).\end{aligned} \tag{3.35}$$

Substituting the solutions (3.22) and (3.23) for $F(r)$ and $G(r)$, respectively, into (3.35) yields the total first-order velocity:

$$\begin{aligned}\boldsymbol{v}_1 = \Big[&\big(-q_f A_1 J_1(q_f r) - \mathrm{i}kB_1 J_1(q_v r)\big)\,2\cos(kz)\boldsymbol{e}_r \\ &+ \big(\mathrm{i}kA_1 J_0(q_f r) + q_v B_1 J_0(q_v r)\big)\,2\mathrm{i}\sin(kz)\boldsymbol{e}_z\Big]\exp(-\mathrm{i}\omega t).\end{aligned} \tag{3.36}$$

3.3. *Constants in terms of the pressure amplitude*

For easier physical interpretation of the constants A_1 and B_1, we express them here in terms of the pressure amplitude p_a at $z = 0$. Using the equation of state (3.3) in combination with the continuity equation (3.2) leads to the following relation:

$$p_1 = -\frac{\mathrm{i}\rho_0 c_f^2}{\omega}\nabla\cdot\boldsymbol{v}_1. \tag{3.37}$$

Applying the solution for the first-order velocity (3.36) to the pressure–velocity relation (3.37) yields the pressure field

$$p_1 = \left[\frac{2\mathrm{i}A_1 k_f^2 \rho_0 c_f^2}{\omega}\right] J_0(q_f r)\cos(kz)\exp(-\mathrm{i}\omega t), \tag{3.38}$$

where the fraction inside the brackets is the amplitude of the pressure field p_1; that is,

$$p_a = \frac{2\mathrm{i}A_1 k_f^2 \rho_0 c_f^2}{\omega}. \tag{3.39}$$

Now, the constant A_1 can be expressed directly from (3.39) as

$$A_1 = -\frac{\mathrm{i}p_a\omega}{2k_f^2\rho_0 c_f^2}. \tag{3.40}$$

The remaining constant follows from combining (3.40) and (3.33):

$$B_1 = \frac{p_a\omega q_f}{2k_f^2\rho_0 c_f^2 k}\frac{J_1(q_f a)}{J_1(q_v a)}. \tag{3.41}$$

Even though we consider only the lowest mode of propagation, the wave is not plane, but, as evident in (3.38), contains r-dependency due to the wave attenuation in the viscous boundary layer. A similar result was also obtained by Qi *et al.* (1995), but their study is restricted to wide channels ($a \gg \delta$).

4. Steady fluid motion at the second order

The steady second-order equations are obtained by time-averaging the equations that follow from the second-order perturbation expansion. The set of the so-called streaming equations comprises the continuity equation

$$\boldsymbol{\nabla} \cdot \langle \boldsymbol{v}_2 \rangle = -\frac{1}{\rho_0} \boldsymbol{\nabla} \cdot \langle \rho_1 \boldsymbol{v}_1 \rangle \tag{4.1}$$

and the momentum equations

$$\boldsymbol{\nabla} \langle p_2 \rangle - \eta \nabla^2 \langle \boldsymbol{v}_2 \rangle - \left(\eta_B + \frac{\eta}{3} \right) \boldsymbol{\nabla} \left(\boldsymbol{\nabla} \cdot \langle \boldsymbol{v}_2 \rangle \right) = -\rho_0 \boldsymbol{\nabla} \cdot \langle \boldsymbol{v}_1 \boldsymbol{v}_1 \rangle \,, \tag{4.2}$$

where the body force on the right-hand side is the spatial variation of the Reynolds stress (Lighthill 1978). The time-average is denoted by

$$\langle \square \rangle = \frac{1}{T} \int_0^T \square \, \mathrm{d}t, \tag{4.3}$$

with the first-order oscillation period T.

The streaming velocity can be decomposed as

$$\langle \boldsymbol{v}_2 \rangle = \boldsymbol{\nabla} \varphi_2 + \boldsymbol{\nabla} \times \boldsymbol{\Psi}_2, \tag{4.4}$$

where φ_2 is the scalar velocity potential and $\boldsymbol{\Psi}_2$ is the divergence-free vector potential. Substituting (4.4) in (4.2) and applying the curl to the resulting equation leads to

$$\nabla^2 \nabla^2 \boldsymbol{\Psi}_2 = -\frac{\rho_0}{\eta} \boldsymbol{\nabla} \times \langle \boldsymbol{v}_1 \cdot \boldsymbol{\nabla} \boldsymbol{v}_1 + \boldsymbol{v}_1 \boldsymbol{\nabla} \cdot \boldsymbol{v}_1 \rangle \,. \tag{4.5}$$

In the process of simplifying the terms on the right-hand side of (4.5), we will use the first-order velocity field (3.35) and the following identities:

$$\sin(k^* z) \cos(kz) = \tfrac{1}{2} [\sin(2k_R z) - \mathrm{i} \sinh(2k_I z)], \tag{4.6}$$

$$\sin(kz) \cos(k^* z) = \tfrac{1}{2} [\sin(2k_R z) + \mathrm{i} \sinh(2k_I z)], \tag{4.7}$$

where k_R and k_I are respectively the real and imaginary part of the wavenumber, and $\square^*$ denotes the complex conjugate of $\square$. Equation (4.5) can now be reformulated into

$$\nabla^2 \nabla^2 \boldsymbol{\Psi}_2 = -\frac{\rho_0}{\eta} \mathrm{Re} \left\{ \sin(2k_R z) \left[R_R(r) + E_R(r) \right] + \mathrm{i} \sinh(2k_I z) \left[R_I(r) + E_I(r) \right] \right\} \boldsymbol{e}_\theta, \tag{4.8}$$

with the functions $R_R(r)$, $R_I(r)$ resulting from the first term in the angle brackets on the right-hand side of (4.5), and the functions $E_R(r)$, $E_I(r)$ originating from the second term. We use separate functions for easier analysis of the individual contributions at a later stage, because the dropping of the second term in the angle brackets on the right-hand side of (4.5) is a very common assumption (e.g. Rayleigh 1884; Schlichting 1932; Lighthill 1978; Doinikov *et al.* 2017). The four functions are given explicitly in appendix C.

The geometry of the problem suggests

$$\boldsymbol{\Psi}_2 = \Psi_2(r, z)\boldsymbol{e}_\theta. \tag{4.9}$$

Substituting (4.9) into (4.8) and eliminating the basis vector yields the following expression:

$$\Delta_\theta^2 \Psi_2 = -\frac{\rho_0}{\eta}\mathrm{Re}\left\{\sin(2k_R z)\left[R_R(r) + E_R(r)\right] + \mathrm{i}\sinh(2k_I z)\left[R_I(r) + E_I(r)\right]\right\}, \tag{4.10}$$

where we applied the operator Δ_θ, defined as

$$\Delta_\theta = \frac{\partial^2}{\partial r^2} + \frac{\partial^2}{\partial z^2} + \frac{1}{r}\frac{\partial}{\partial r} - \frac{1}{r^2}. \tag{4.11}$$

Based on the right-hand side of (4.10), we assume

$$\Psi_2(r, z) = -\frac{\rho_0}{\eta}\mathrm{Re}\left\{\sin(2k_R z)S_R(r) + \mathrm{i}\sinh(2k_I z)S_I(r)\right\}, \tag{4.12}$$

with the unknown functions $S_R(r)$ and $S_I(r)$. Substituting (4.12) into (4.10) gives two ordinary fourth-order differential equations,

$$\begin{aligned}&\frac{\mathrm{d}^4 S_R(r)}{\mathrm{d}r^4} + \frac{2}{r}\frac{\mathrm{d}^3 S_R(r)}{\mathrm{d}r^3} + \left(-\frac{3}{r^2} - 8k_R^2\right)\frac{\mathrm{d}^2 S_R(r)}{\mathrm{d}r^2} + \left(\frac{3}{r^3} - \frac{8k_R^2}{r}\right)\frac{\mathrm{d}S_R(r)}{\mathrm{d}r}\\ &\quad + \left(-\frac{3}{r^4} + \frac{8k_R^2}{r^2} + 16k_R^4\right)S_R(r) = R_R(r) + E_R(r),\end{aligned} \tag{4.13}$$

$$\begin{aligned}&\frac{\mathrm{d}^4 S_I(r)}{\mathrm{d}r^4} + \frac{2}{r}\frac{\mathrm{d}^3 S_I(r)}{\mathrm{d}r^3} + \left(-\frac{3}{r^2} + 8k_I^2\right)\frac{\mathrm{d}^2 S_I(r)}{\mathrm{d}r^2} + \left(\frac{3}{r^3} + \frac{8k_I^2}{r}\right)\frac{\mathrm{d}S_I(r)}{\mathrm{d}r}\\ &\quad + \left(-\frac{3}{r^4} - \frac{8k_I^2}{r^2} + 16k_I^4\right)S_I(r) = R_I(r) + E_I(r),\end{aligned} \tag{4.14}$$

which we must solve in order to find the stream function $\Psi_2(r, z)$. In the process, it will be convenient to define the linear differential operator

$$\Delta_1 = \frac{\mathrm{d}^2}{\mathrm{d}r^2} + \frac{1}{r}\frac{\mathrm{d}}{\mathrm{d}r} - \frac{1}{r^2} \tag{4.15}$$

and use it to transform (4.13) and (4.14) into

$$\Delta_1\Delta_1 S_R(r) - 8k_R^2\Delta_1 S_R(r) + 16k_R^4 S_R(r) = R_R(r) + E_R(r) \tag{4.16}$$

and

$$\Delta_1\Delta_1 S_I(r) + 8k_I^2\Delta_1 S_I(r) + 16k_I^4 S_I(r) = R_I(r) + E_I(r), \tag{4.17}$$

respectively.

To solve (4.16) and (4.17), we will make use of the linear finite Hankel transform of order one (introduced by Sneddon 1946, 1972), which is defined as

$$\mathcal{H}_1\{f(r)\} = \int_0^b rf(r)J_1(\xi_i r)\,\mathrm{d}r = \bar{f}(\xi_i) \tag{4.18}$$

for a function $f(r)$ integrable on the interval $0 \leqslant r \leqslant b$. The corresponding inverse transform follows as

$$\mathcal{H}_1^{-1}\left\{\bar{f}(\xi_i)\right\} = f(r) = \frac{2}{b^2}\sum_{i=1}^{\infty}\bar{f}(\xi_i)\frac{J_1(\xi_i r)}{[J_2(\xi_i b)]^2}, \tag{4.19}$$

with $\bar{\square}$ denoting the transformed expression, and provided that ξ_i with $i = 1, 2, 3, \ldots$ are the positive roots of the transcendental equation

$$J_1(\xi_i b) = 0. \tag{4.20}$$

The transformation of Δ_1 that is applied to a function $f(r)$ gives (Sneddon 1946, 1972)

$$\mathcal{H}_1\{\Delta_1 f(r)\} = -\xi_i^2\bar{f}(\xi_i) + b\xi_i f(b)J_2(\xi_i b). \tag{4.21}$$

Applying the finite Hankel transform defined in (4.18) to the differential (4.16), limiting the domain of transformation with the radius of the tube a, and exploiting the property specified in (4.21) yields

$$\begin{aligned}\xi_i^4\bar{S}_R(\xi_i) - a\xi_i^3 S_R(r)\big|_{r=a}J_2(\xi_i a) + 8k_R^2\xi_i^2\bar{S}_R(\xi_i) + a\xi_i\Delta_1 S_R(r)\big|_{r=a}J_2(\xi_i a)\\ +8k_R^2 a\xi_i S_R(r)\big|_{r=a} + 16k_R^4\bar{S}_R(\xi_i) = \bar{R}_R(\xi_i) + \bar{E}_R(\xi_i).\end{aligned} \tag{4.22}$$

The transformed unknown function $\bar{S}_R(\xi_i)$ can be expressed from (4.22) as

$$\bar{S}_R(\xi_i) = \frac{1}{(\xi_i^2 + 4k_R^2)^2}[\bar{R}_R(\xi_i) + \bar{E}_R(\xi_i) - a\xi_i C_1 J_2(\xi_i a) + a\xi_i C_2(\xi_i^2 J_2(\xi_i a) - 8k_R^2)], \tag{4.23}$$

with the constants C_1 and C_2 defined as

$$C_1 = \Delta_1 S_R(r)\big|_{r=a}, \tag{4.24}$$

$$C_2 = S_R(r)\big|_{r=a}. \tag{4.25}$$

The function $S_R(r)$ can be obtained by applying the inverse transform (4.19)–(4.23), i.e.

$$\begin{aligned}S_R(r) = \frac{2}{a^2}\sum_{i=1}^{\infty}\frac{J_1(\xi_i r)}{[J_2(\xi_i a)]^2(\xi_i^2 + 4k_R^2)^2}[\bar{R}_R(\xi_i) + \bar{E}_R(\xi_i)\\ - a\xi_i C_1 J_2(\xi_i a) + a\xi_i C_2(\xi_i^2 J_2(\xi_i a) - 8k_R^2)].\end{aligned} \tag{4.26}$$

The second unknown function, $S_I(r)$, can be obtained by applying an analogous procedure to the differential equation (4.17). The resulting expression can be written as

$$\begin{aligned}S_I(r) = \frac{2}{a^2}\sum_{i=1}^{\infty}\frac{J_1(\xi_i r)}{[J_2(\xi_i a)]^2(\xi_i^2 - 4k_I^2)^2}[\bar{R}_I(\xi_i) + \bar{E}_I(\xi_i)\\ - a\xi_i C_3 J_2(\xi_i a) + a\xi_i C_4(\xi_i^2 J_2(\xi_i a) + 8k_I^2)],\end{aligned} \tag{4.27}$$

where the constants are defined as

$$C_3 = \Delta_1 S_I(r)\big|_{r=a}, \tag{4.28}$$

$$C_4 = S_I(r)\big|_{r=a}. \tag{4.29}$$

Returning to the decomposition of the streaming velocity (4.4) and substituting it into (4.1) leads to

$$\nabla^2\varphi_2 = -\frac{1}{\rho_0}\left\langle \boldsymbol{v}_1 \cdot \boldsymbol{\nabla}\rho_1 + \rho_1 \boldsymbol{\nabla}\cdot \boldsymbol{v}_1 \right\rangle. \tag{4.30}$$

Using the first-order velocity field (3.35), the first-order pressure field (3.38), the equation of state (3.3) and the identities

$$\cos(k^* z)\cos(kz) = \tfrac{1}{2}[\cos(2k_R z) + \cosh(2k_I z)], \tag{4.31}$$

$$\sin(k^* z)\sin(kz) = \tfrac{1}{2}[-\cos(2k_R z) + \cosh(2k_I z)] \tag{4.32}$$

transforms (4.30) into

$$\nabla^2\varphi_2 = -\frac{p_a}{2\rho_0 c_f}\mathrm{Re}\left\{\cos(2k_R z)M_R(r) + \cosh(2k_I z)M_I(r)\right\}, \tag{4.33}$$

with the source terms $M_R(r)$ and $M_I(r)$ given in appendix D. We assume, based on (4.33), that the solution has the following form:

$$\varphi_2(r,z) = -\frac{p_a}{2\rho_0 c_f}\mathrm{Re}\left\{\cos(2k_R z)U_R(r) + \cosh(2k_I z)U_I(r)\right\}. \tag{4.34}$$

The unknown functions $U_R(r)$ and $U_I(r)$ can be obtained by solving two differential equations that follow from substituting (4.34) into (4.33), namely

$$\frac{\mathrm{d}^2 U_R(r)}{\mathrm{d}r^2} + \frac{1}{r}\frac{\mathrm{d}U_R(r)}{\mathrm{d}r} - 4k_R^2 U_R(r) = M_R(r) \tag{4.35}$$

and

$$\frac{\mathrm{d}^2 U_I(r)}{\mathrm{d}r^2} + \frac{1}{r}\frac{\mathrm{d}U_I(r)}{\mathrm{d}r} + 4k_I^2 U_I(r) = M_I(r). \tag{4.36}$$

The general solutions to the homogeneous equations related to (4.35) and (4.36), denoted by the superscript $\square^H$, follow as

$$U_R^H(r) = C_5 J_0(2\mathrm{i}k_R r) + C_6 Y_0(-2\mathrm{i}k_R r) \tag{4.37}$$

and

$$U_I^H(r) = C_7 J_0(2k_I r) + C_8 Y_0(2k_I r), \tag{4.38}$$

respectively, with the unknown constants C_5, C_6, C_7, C_8. The particular solutions to (4.35) and (4.36), denoted by the superscript $\square^P$, are obtained by the method of variation of

parameters (e.g. Boyce, DiPrima & Meade 2017), and follow as

$$U_R^P(r) = -\frac{\pi}{2}J_0(2\mathrm{i}k_R r)\int_0^r xM_R(x)Y_0(-2\mathrm{i}k_R x)\,\mathrm{d}x + \frac{\pi}{2}Y_0(-2\mathrm{i}k_R r)\int_0^r xM_R(x)J_0(2\mathrm{i}k_R x)\,\mathrm{d}x \tag{4.39}$$

and

$$U_I^P(r) = -\frac{\pi}{2}J_0(2k_I r)\int_0^r xM_I(x)Y_0(2k_I x)\,\mathrm{d}x + \frac{\pi}{2}Y_0(2k_I r)\int_0^r xM_I(x)J_0(2k_I x)\,\mathrm{d}x, \tag{4.40}$$

respectively. The general solutions to (4.35) and (4.36) are sums of solutions to the related homogeneous equations, $U_R^H(r)$ and $U_I^H(r)$, and of particular solutions, $U_R^P(r)$ and $U_I^P(r)$. Therefore, the general solutions are given as

$$U_R(r) = -\frac{\pi}{2}J_0(2\mathrm{i}k_R r)\int_0^r xM_R(x)Y_0(-2\mathrm{i}k_R x)\,\mathrm{d}x + \frac{\pi}{2}Y_0(-2\mathrm{i}k_R r)\int_0^r xM_R(x)J_0(2\mathrm{i}k_R x)\,\mathrm{d}x + C_5 J_0(2\mathrm{i}k_R r) \tag{4.41}$$

and

$$U_I(r) = -\frac{\pi}{2}J_0(2k_I r)\int_0^r xM_I(x)Y_0(2k_I x)\,\mathrm{d}x + \frac{\pi}{2}Y_0(2k_I r)\int_0^r xM_I(x)J_0(2k_I x)\,\mathrm{d}x + C_7 J_0(2k_I r), \tag{4.42}$$

where we applied $C_6 = 0$ and $C_8 = 0$, since the solution has to remain finite at $r = 0$.

4.1. *Streaming velocity*

The streaming velocity $\langle \boldsymbol{v}_2 \rangle$ from (4.4) can be expressed in terms of the functions $S_R(r)$, $S_I(r)$, $U_R(r)$ and $U_I(r)$ as

$$\begin{aligned}\langle \boldsymbol{v}_2 \rangle = {} & \mathrm{Re}\left\{\cos(2k_R z)\left[\frac{2\rho_0 k_R}{\eta}S_R(r) - \frac{p_a}{2\rho_0 c_f^2}\frac{\mathrm{d}U_R(r)}{\mathrm{d}r}\right]\right. \\ & \left. + \cosh(2k_I z)\left[\mathrm{i}\frac{2\rho_0 k_I}{\eta}S_I(r) - \frac{p_a}{2\rho_0 c_f^2}\frac{\mathrm{d}U_I(r)}{\mathrm{d}r}\right]\right\}\boldsymbol{e}_r \\ & - \mathrm{Re}\left\{\sin(2k_R z)\left[\frac{\rho_0}{\eta}\frac{1}{r}S_R(r) + \frac{\rho_0}{\eta}\frac{\mathrm{d}S_R(r)}{\mathrm{d}r} - \frac{p_a k_R}{\rho_0 c_f^2}U_R(r)\right]\right. \\ & \left. + \sinh(2k_I z)\left[\mathrm{i}\frac{\rho_0}{\eta}\frac{1}{r}S_I(r) + \mathrm{i}\frac{\rho_0}{\eta}\frac{\mathrm{d}S_I(r)}{\mathrm{d}r} + \frac{p_a k_I}{\rho_0 c_f^2}U_I(r)\right]\right\}\boldsymbol{e}_z,\end{aligned} \tag{4.43}$$

where the derivatives $\mathrm{d}S_R(r)/\mathrm{d}r$, $\mathrm{d}S_I(r)/\mathrm{d}r$, $\mathrm{d}U_R(r)/\mathrm{d}r$, $\mathrm{d}U_I(r)/\mathrm{d}r$ follow from (4.26), (4.27), (4.41), (4.42), respectively, and are given in appendix E.

The expression (4.43) is a time-averaged Eulerian streaming velocity, which has often been the final result of classical studies (e.g. Rayleigh 1884; Schlichting 1932; Schuster & Matz 1940). However, the observable behaviour of the fluid undergoing streaming, e.g. by particle image velocimetry (Wiklund, Green & Ohlin 2012), is better represented by the time-averaged Lagrangian velocity (Westervelt 1953) or by the average mass transport velocity (Nyborg 1965). The time-averaged Lagrangian velocity is defined as

$$\langle \boldsymbol{v}_2 \rangle^L = \langle \boldsymbol{v}_2 \rangle + \boldsymbol{v}_{SD}, \tag{4.44}$$

where $\boldsymbol{v}_{SD}$ is the Stokes drift,

$$\boldsymbol{v}_{SD} = \left\langle \left(\int \boldsymbol{v}_1 \,\mathrm{d}t \cdot \boldsymbol{\nabla} \right) \boldsymbol{v}_1 \right\rangle, \tag{4.45}$$

given in appendix F. The average mass transport velocity follows as

$$\langle \boldsymbol{v}_2 \rangle^M = \langle \boldsymbol{v}_2 \rangle + \frac{1}{\rho_0} \langle \rho_1 \boldsymbol{v}_1 \rangle, \tag{4.46}$$

and is divergence-free, which follows from (4.1). Using (3.3), (3.38) and (3.36), together with (4.46), leads to

$$\begin{aligned}
\langle \boldsymbol{v}_2 \rangle^M = \mathrm{Re}\Bigg\{ & \cos(2k_R z)\left[\frac{2\rho_0 k_R}{\eta} S_R(r) - \frac{p_a}{2\rho_0 c_f^2}\left(\frac{\mathrm{d}U_R(r)}{\mathrm{d}r}\right.\right. \\
& \left.\left. + q_f A_1 J_1(q_f r) J_0(q_f^* r) + \mathrm{i}kB_1 J_1(q_v r) J_0(q_f^* r)\right)\right] \\
& + \cosh(2k_I z)\left[\mathrm{i}\frac{2\rho_0 k_I}{\eta} S_I(r) - \frac{p_a}{2\rho_0 c_f^2}\left(\frac{\mathrm{d}U_I(r)}{\mathrm{d}r}\right.\right. \\
& \left.\left. + q_f A_1 J_1(q_f r) J_0(q_f^* r) + \mathrm{i}kB_1 J_1(q_v r) J_0(q_f^* r)\right)\right]\Bigg\} \boldsymbol{e}_r \\
& - \mathrm{Re}\Bigg\{ \sin(2k_R z)\left[\frac{\rho_0}{\eta}\frac{1}{r} S_R(r) + \frac{\rho_0}{\eta}\frac{\mathrm{d}S_R(r)}{\mathrm{d}r} - \frac{p_a}{\rho_0 c_f^2}\left(k_R U_R(r)\right.\right. \\
& \left.\left. - \frac{kA_1}{2} J_0(q_f r) J_0(q_f^* r) + \mathrm{i}\frac{q_v B_1}{2} J_0(q_v r) J_0(q_f^* r)\right)\right] \\
& + \sinh(2k_I z)\left[\mathrm{i}\frac{\rho_0}{\eta}\frac{1}{r} S_I(r) + \mathrm{i}\frac{\rho_0}{\eta}\frac{\mathrm{d}S_I(r)}{\mathrm{d}r} + \frac{p_a}{\rho_0 c_f^2}\left(k_I U_I(r)\right.\right. \\
& \left.\left. + \mathrm{i}\frac{kA_1}{2} J_0(q_f r) J_0(q_f^* r) + \frac{q_v B_1}{2} J_0(q_v r) J_0(q_f^* r)\right)\right]\Bigg\} \boldsymbol{e}_z.
\end{aligned} \tag{4.47}$$

4.2. *Unknown constants at the second order*

To find the constants C_1, C_2, C_3, C_4, C_5 and C_7 appearing in (4.26), (4.27), (4.41) and (4.42), we apply the no-slip boundary condition at the wall. The condition is imposed by

fixing the time-averaged Lagrangian streaming velocity (4.44) to zero at $r = a$. However, the assumption of a rigid wall leads to zero first-order velocity at $r = a$, and consequently to $\boldsymbol{v}_{SD} = 0$ at $r = a$. Therefore, the no-slip boundary condition can be imposed by setting the Eulerian streaming velocity (4.43) to zero at $r = a$.

This leads to four equations, namely

$$\frac{2\rho_0 k_R}{\eta} S_R(r) - \frac{p_a}{2\rho_0 c_f^2} \frac{\mathrm{d}U_R(r)}{\mathrm{d}r} = 0 \quad \text{at } r = a, \tag{4.48}$$

$$\mathrm{i}\frac{2\rho_0 k_I}{\eta} S_I(r) - \frac{p_a}{2\rho_0 c_f^2} \frac{\mathrm{d}U_I(r)}{\mathrm{d}r} = 0 \quad \text{at } r = a, \tag{4.49}$$

from the r-component of the streaming velocity, and

$$\frac{\rho_0}{\eta}\frac{1}{r} S_R(r) + \frac{\rho_0}{\eta}\frac{\mathrm{d}S_R(r)}{\mathrm{d}r} - \frac{p_a k_R}{\rho_0 c_f^2} U_R(r) = 0 \quad \text{at } r = a, \tag{4.50}$$

$$\mathrm{i}\frac{\rho_0}{\eta}\frac{1}{r} S_I(r) + \mathrm{i}\frac{\rho_0}{\eta}\frac{\mathrm{d}S_I(r)}{\mathrm{d}r} + \frac{p_a k_I}{\rho_0 c_f^2} U_I(r) = 0 \quad \text{at } r = a, \tag{4.51}$$

from the z-component.

Since (4.26) and (4.27) contain a factor of $J_1(\xi_i r)$ that evaluates to zero for every ξ_i at $r = a$, $S_R(r)$ and $S_I(r)$ are also zero at $r = a$ by definition. The constants C_2 and C_4 then follow trivially from their definitions (4.25) and (4.29), respectively:

$$C_2 = 0, \tag{4.52}$$

$$C_4 = 0. \tag{4.53}$$

From (4.49) and (4.51), we obtain

$$C_5 = \frac{\pi}{2}\int_0^a x M_R(x) Y_0(-2\mathrm{i}k_R x)\,\mathrm{d}x + \frac{\pi}{2}\frac{Y_1(-2\mathrm{i}k_R a)}{J_1(2\mathrm{i}k_R a)}\int_0^a x M_R(x) J_0(2\mathrm{i}k_R x)\,\mathrm{d}x, \tag{4.54}$$

$$C_7 = \frac{\pi}{2}\int_0^a x M_I(x) Y_0(2k_I x)\,\mathrm{d}x - \frac{\pi}{2}\frac{Y_1(2k_I a)}{J_1(2k_I a)}\int_0^a x M_I(x) J_0(2k_I x)\,\mathrm{d}x. \tag{4.55}$$

Exploiting, again, that $S_R(r)$ and $S_I(r)$ are zero at $r = a$, together with boundary conditions (4.50) and (4.51), yields the last two constants in the following form:

$$C_1 = \frac{a}{\sum_{i=1}^{\infty} \xi_i^2 \left(\xi_i^2 + 4k_R^2\right)^{-2}} \left\{ \sum_{i=1}^{\infty} \frac{\xi_i \left[\bar{R}_R(\xi_i) + \bar{E}_R(\xi_i)\right]}{a^2 J_2(\xi_i a)\left(\xi_i^2 + 4k_R^2\right)^2} + \frac{\pi}{4}\frac{p_a \eta k_R}{\rho_0^2 c_f^2}\left[Y_0(-2\mathrm{i}k_R a) + \frac{J_0(2\mathrm{i}k_R a)}{J_1(2\mathrm{i}k_R a)} Y_1(-2\mathrm{i}k_R a)\right]\int_0^a x M_R(x) J_0(2\mathrm{i}k_R x)\,\mathrm{d}x \right\}, \tag{4.56}$$

$$C_3 = \frac{a}{\sum_{i=1}^{\infty} \xi_i^2 \left(\xi_i^2 - 4k_I^2\right)^{-2}} \left\{ \sum_{i=1}^{\infty} \frac{\xi_i \left[\bar{R}_I(\xi_i) + \bar{E}_I(\xi_i)\right]}{a^2 J_2(\xi_i a)\left(\xi_i^2 - 4k_I^2\right)^2} + \mathrm{i}\frac{\pi}{4}\frac{p_a \eta k_I}{\rho_0^2 c_f^2}\left[Y_0(2k_I a) - \frac{J_0(2k_I a)}{J_1(2k_I a)} Y_1(2k_I a)\right]\int_0^a x M_I(x) J_0(2k_I x)\,\mathrm{d}x \right\}. \tag{4.57}$$

Fluid	ρ_0 (kg m^{-3})	c_f (m s^{-1})	η (Pa s)	η_B (Pa s)	δ (μm) at $f = 100$ kHz	λ (mm) at $f = 100$ kHz
Water	996.6	1502	8.538×10^{-4}	2.4×10^{-3}	1.65	15.0
Oil	922.6	1445	4.153×10^{-2}	8.3×10^{-2}	12.0	14.5
Glycerol	1261.34	1920	1.410×10^{0}	2.0×10^{0}	59.7	19.2
Air	1.161	347.4	1.854×10^{-5}	1.1×10^{-5}	7.13	3.47

Table 1. Material properties of the fluids used in the numerical analysis (Miner & Dalton 1953; Hirai & Eyring 1958; Karlsen & Bruus 2015).

5. Streaming analysis

Here, we analyse the acoustic streaming for multiple combinations of material, geometrical and wave properties in a tube excited with two opposing decaying travelling waves that form a pseudo-standing wave. The analysis is performed in Mathematica 12.0 (Wolfram Research, Inc., 2019). The expressions (4.43), (4.44) and (4.47) for the velocity fields are used together with (4.26), (4.27), (4.41), (4.42), (F1), and the constants (4.52), (4.53), (4.54), (4.55), (4.56), (4.57). The integrals appearing in the transformed source terms $\bar{R}_R(\xi_i)$, $\bar{R}_I(\xi_i)$, $\bar{E}_R(\xi_i)$, $\bar{E}_I(\xi_i)$, and in the expressions $U_R(r)$, $U_I(r)$, are evaluated numerically. The Mathematica Notebook file with the implementations of all necessary expressions for evaluation of arbitrary streaming fields is available as supplementary material at https://doi.org/10.1017/jfm.2020.1046. The infinite sums associated with the solution are truncated at i_{max} (usually at 200), at which the streaming velocity field is sufficiently converged. The limit is determined through convergence studies, information on which is given in appendix B.

In our analysis, we use water, oil, glycerol and air. The material properties of all four fluids are given in table 1.

5.1. *Definitions*

To improve understanding of the fluid behaviour at the first order, we show, in figure 2, the real and the imaginary part of the wavenumber. In addition, the first-order pressure profile is given in figure 3, which indicates the symmetry of the pseudo-standing pressure wave with respect to the $z = 0$ plane. The amplitude decay relates to the imaginary part (k_I) of the wavenumber, while the change of the wavelength with tube radius relates to the real part (k_R) of the wavenumber. For the liquids, we will use a pressure amplitude of 100 kPa, which corresponds to the usual pressure amplitudes in acoustofluidic systems (Barnkob *et al.* 2010). In the case of air, the usual pressure amplitude is much lower, up to 1 kPa (Schuster & Matz 1940; Imani & Robert 2015), which is the value that will be used for the results presented in appendix A.

The first velocity node is positioned at $z = 0$, which is also a plane of symmetry of our pseudo-standing pressure wave (as indicated in figure 3). Since the fluid is viscous and bounded, the actual wavelength is defined as $\lambda_R = 2\pi/k_R$. The velocity node therefore repeats with a period of $\lambda_R/2$. The velocity antinode is in this case positioned at $z = \lambda_R/4$, and repeats with the same period as the node. Even though the fluids in our analysis are viscous (i.e. the imaginary part of the wavenumber k is nonzero), we will use the acoustic wavelength of an unbounded ideal fluid λ, defined as $\lambda = c_f/f$, for a more generalized analysis.

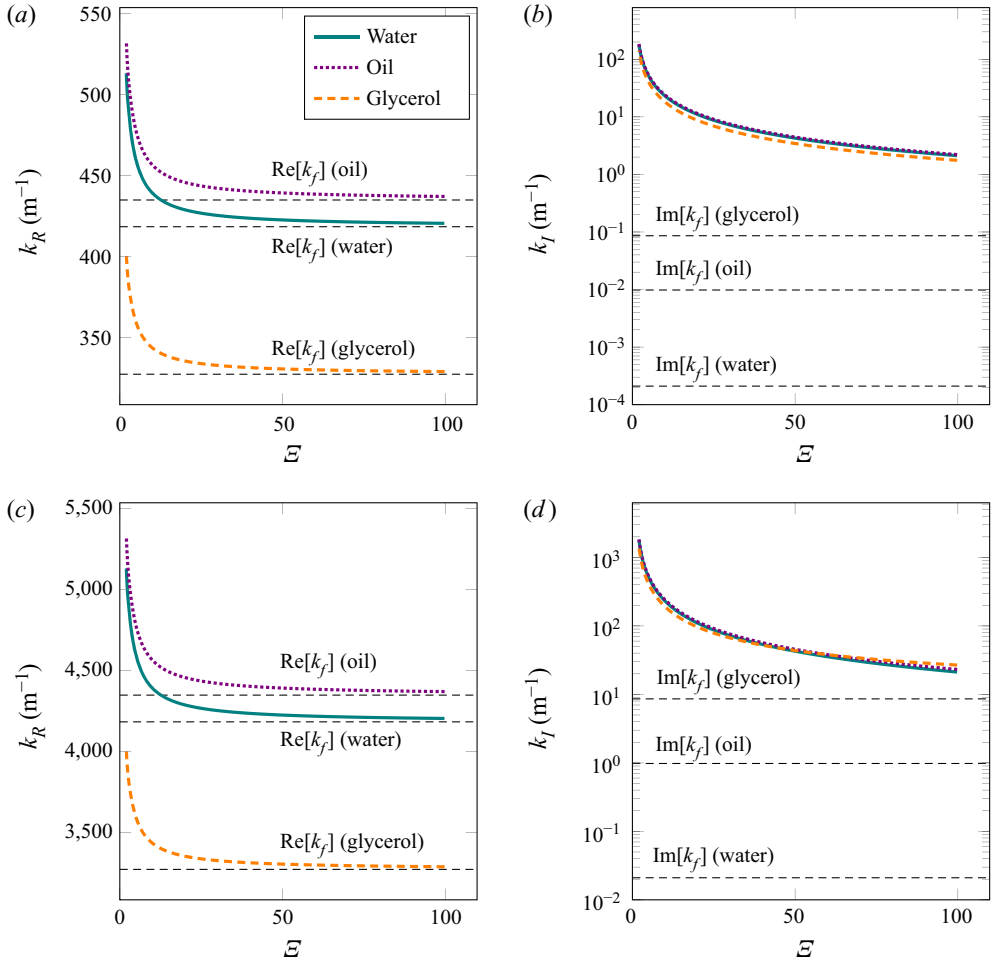

Figure 2. The real and imaginary parts of the wavenumber according to (3.31) and (3.32), respectively, for water, oil and glycerol: (*a*) k_R at $f = 100$ kHz; (*b*) k_I at $f = 100$ kHz; (*c*) k_R at $f = 1$ MHz; (*d*) k_I at $f = 1$ MHz. The dimensionless ratio $\Xi = a/\delta$ represents the varying tube radius relative to the viscous boundary layer thickness. The real and imaginary parts of the wavenumber in an unbounded fluid domain k_f are plotted for reference.

The second-order solution is also symmetric about the $z = 0$ plane, which follows from the analysis of the z-dependency of the streaming velocity fields (4.43) and (4.47). The streaming patterns will therefore be analysed on the interval $0 \leq z \leq \lambda$. When a large-scale behaviour is analysed, the interval of analysis will be increased to $0 \leq z \leq 4\lambda$.

In continuation, we will distinguish between two types of streaming vortices, namely Rayleigh streaming and Schlichting streaming. The Rayleigh streaming vortex denotes the flow from the velocity node towards the antinode near the axis of the tube, and the oppositely directed flow near the wall. The Schlichting streaming vortex represents the flow in the direction opposite to that of the Rayleigh streaming, and appears between the Rayleigh streaming and the wall. The two types of streaming are also shown in figure 4. The streaming vortices are analysed on a single rz-plane, as the problem is axisymmetric. However, when three-dimensional geometry is considered these vortices extend through the whole range of θ, namely $0 \leqslant \theta < 2\pi$, and are of toroidal shape. The two types of

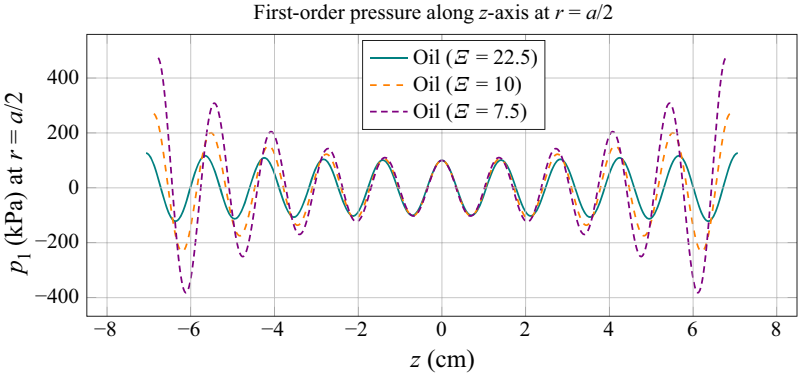

Figure 3. The first-order pressure in oil along the z-axis, at $r = a/2$, for $f = 100$ kHz and $p_a = 100$ kPa. The dimensionless ratio $\Xi = a/\delta$ represents the varying tube radius relative to the viscous boundary layer thickness of $\delta = 12$ μm. For each radius of the tube, we plot the pressure in the range of $-5\lambda_R < z < 5\lambda_R$, with $\lambda_R = 2\pi/k_R$.

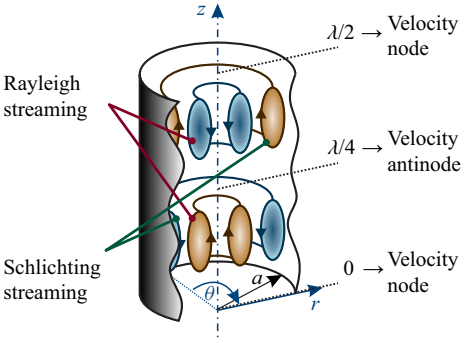

Figure 4. The terminology used for different types of streaming vortices. Rayleigh streaming denotes the fluid flow from the velocity node to the antinode near the axis of the tube, and the flow in the opposite direction near the wall. Schlichting streaming denotes the flow in the direction opposite to that of the Rayleigh streaming.

streaming vortices are boundary-driven, and are normally confined between a velocity nodal plane and antinodal plane of an acoustic field. However, we will also encounter streaming driven by the decaying travelling wave grazing the wall (Nyborg 1965, p. 274). This type of large-scale (with respect to λ) streaming will be called Eckart-like streaming, after Eckart (1948), who theoretically investigated the streaming driven by the attenuation of a travelling wave in the bulk of a fluid, extending over several acoustic wavelengths in the direction of the wave propagation. This happens, for example, when the waveguide of an acoustic beam is wider than the acoustic wavelength (Boluriaan & Morris 2003).

We will often refer to the ratio of a tube radius to the thickness of the viscous boundary layer, i.e. the quantity

$$\Xi = \frac{a}{\delta}. \tag{5.1}$$

The critical ratio Ξ_S, as indicated in figure 5, denotes the transition between the Rayleigh-plus-Schlichting streaming regime to the Schlichting-only streaming regime. It is defined as the value of Ξ at which the axial component of the streaming velocity changes direction, at $z = \lambda_R/8$. We will also use another dimensionless parameter, the ratio of the

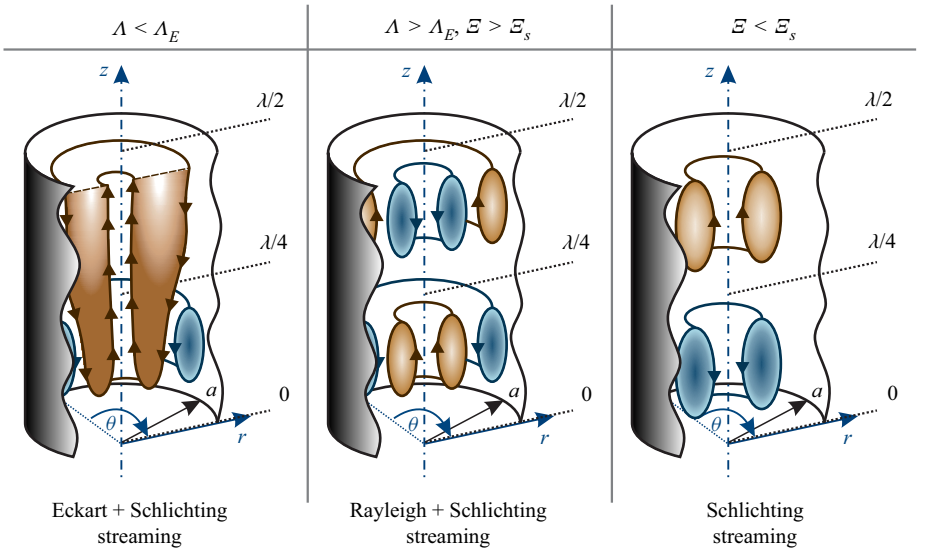

Figure 5. Visual explanation of the critical values of $\Xi = a/\delta$ and $\Lambda = \lambda/a$ used in the analysis. In the case of $\Xi < \Xi_S$ the Rayleigh streaming disappears completely, and only the Schlichting streaming remains. This happens when the axial component of the streaming at the axis, at $z = \lambda_R/8$, changes direction. When $\Lambda < \Lambda_E$, large-scale Eckart-like streaming begins to develop near the axis of the tube. The ratio Λ_E is defined as the value of Λ at which the axial streaming velocity at the axis, evaluated at $z = 3\lambda_R/8$, changes direction, while $\Xi > \Xi_S$.

acoustic wavelength to the tube radius, i.e. the quantity

$$\Lambda = \frac{\lambda}{a}. \tag{5.2}$$

The critical ratio Λ_E signifies the transition between the Rayleigh-plus-Schlichting streaming regime to the Eckart-plus-Schlichting regime, and is defined as the value of Λ at which the axial component of the streaming velocity changes direction, at $z = 3\lambda_R/8$, while Ξ is sufficiently above Ξ_S so that the transition associated with Ξ_S does not interfere. The specified critical values of Ξ and Λ, depicted in figure 5, are problem-specific parameters, and their dependency on the material properties and on the excitation frequency will be investigated in the following sections. The superscript $\square^M$ indicates that the ratio is determined via the average mass transport velocity (4.47), while critical ratios without the superscript are determined via the Eulerian streaming velocity (4.43).

5.2. *The evolution of streaming patterns*

Figure 6 shows the evolution of the average mass transport velocity patterns inside an oil-filled tube with respect to the decreasing tube radius at a constant frequency of $f = 100$ kHz, which corresponds to a viscous boundary layer thickness of $\delta = 12$ μm and an acoustic wavelength of $\lambda = 14.45$ mm. We observe a qualitative change in the behaviour. First, at $a = 270$ μm ($\Xi = 22.5$), in figure 6(*a*), we see a combination of smaller Schlichting vortices at the wall and dominant Rayleigh streaming vortices that agree with well-known experiments (see Andrade 1931); i.e. the fluid flows from the velocity node towards the antinode near the axis of the tube and in the opposite direction

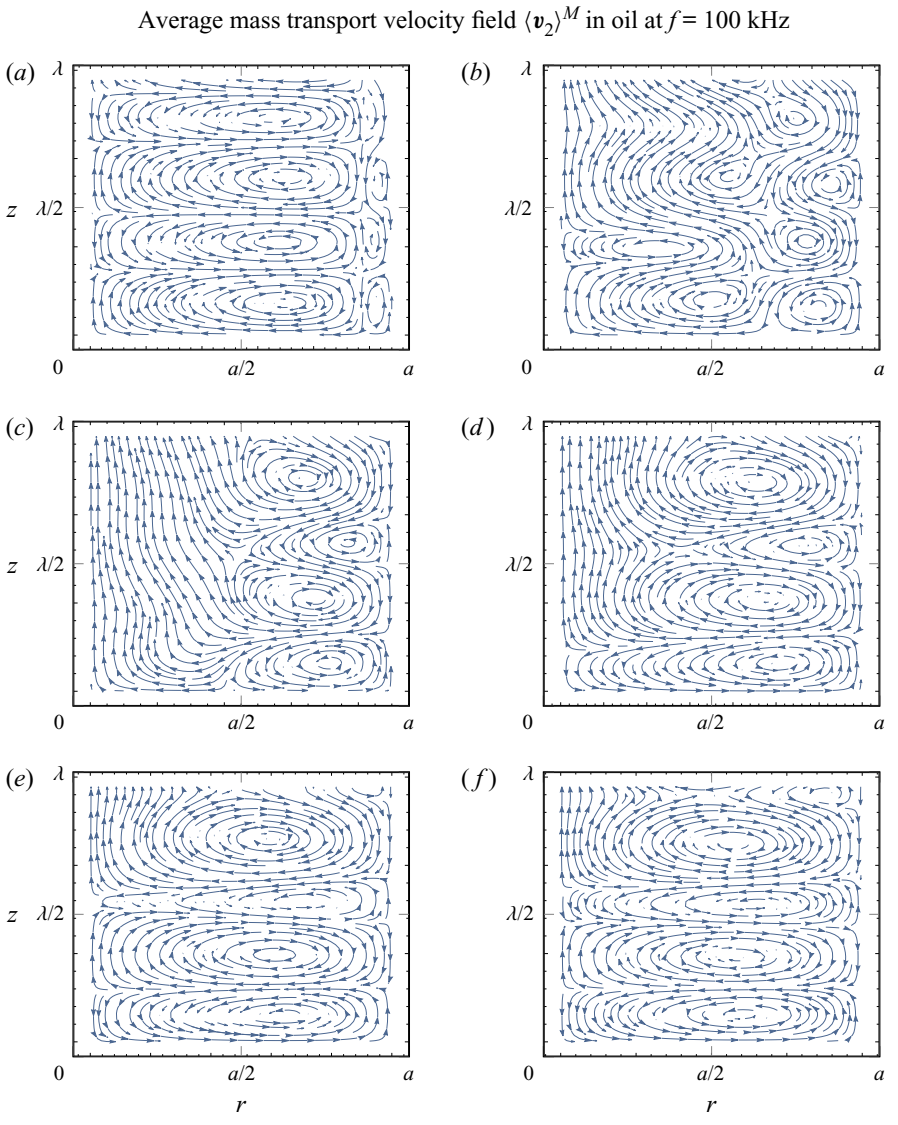

Figure 6. The average mass transport velocity patterns in oil, for a tube radius of (*a*) $a = 270$ μm ($\Xi = 22.5$), (*b*) $a = 120$ μm ($\Xi = 10$), (*c*) $a = 90$ μm ($\Xi = 7.5$), (*d*) $a = 70$ μm ($\Xi = 5.83$), (*e*) $a = 50$ μm ($\Xi = 4.17$) and (*f*) $a = 40$ μm ($\Xi = 3.33$), for $f = 100$ kHz. The corresponding acoustic wavelength is $\lambda = 14.45$ mm, while the actual wavelength is 14.14 mm $\geqslant \lambda_R \geqslant$ 12.67 mm. The viscous boundary layer has a thickness of $\delta = 12$ μm. The first velocity node is at $z = 0$, while the first velocity antinode appears at $z = \lambda_R/4$. Arrows indicate the direction of the flow.

near the wall. When the radius is decreased to $a = 120$ μm ($\Xi = 10$) and $a = 90$ μm ($\Xi = 7.5$), we observe the expansion of the Schlichting vortices near the wall, in addition to the shrinking of the Rayleigh vortices (figure 6*b*,*c*). Further decreasing the radius to $a = 70$ μm ($\Xi = 5.83$), $a = 50$ μm ($\Xi = 4.17$) and $a = 40$ μm ($\Xi = 3.33$) reveals the disappearance of the Rayleigh streaming, while the Schlichting streaming spreads throughout the whole radius of the tube (figure 6*d*–*f*). Figure 7 gives the Eulerian streaming velocity patterns corresponding to the same cases as presented in figure 6.

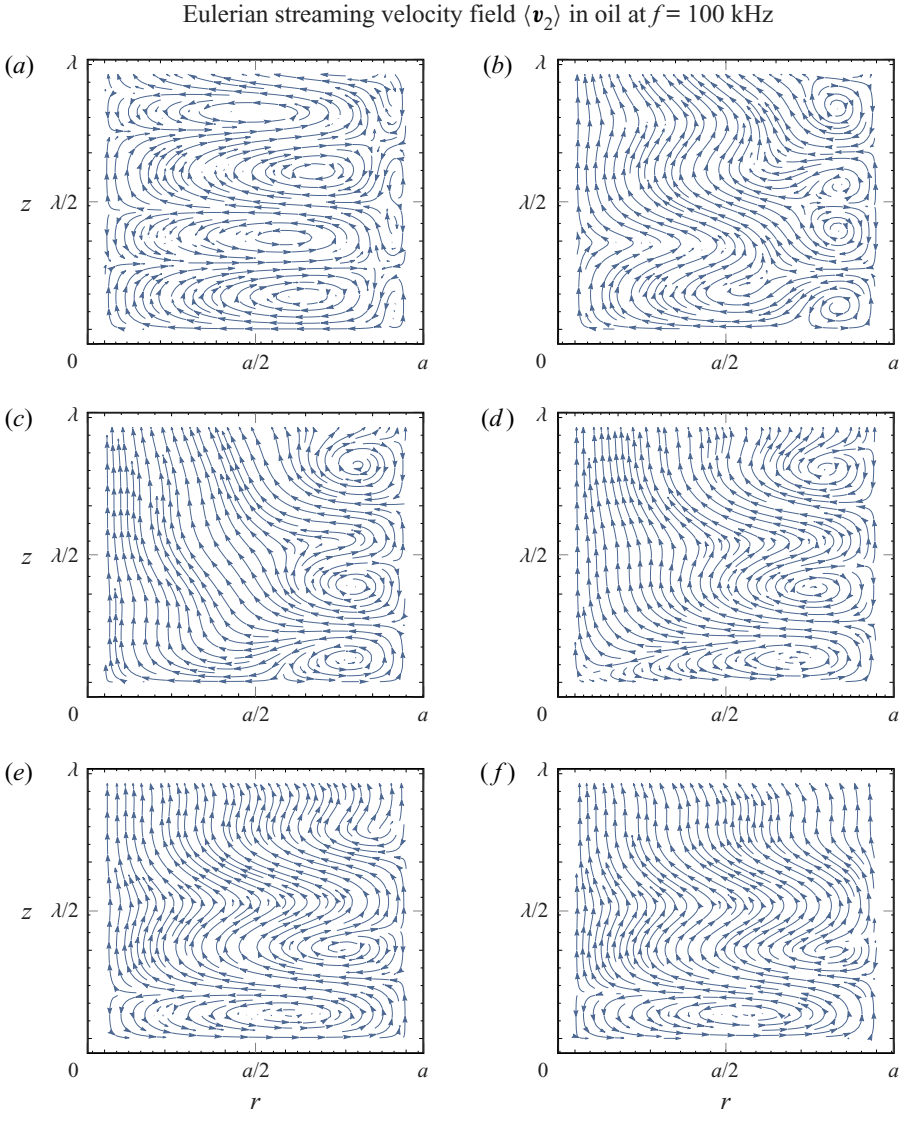

Figure 7. The Eulerian streaming velocity patterns in oil, for a tube radius of (*a*) $a = 270$ μm ($\Xi = 22.5$), (*b*) $a = 120$ μm ($\Xi = 10$), (*c*) $a = 90$ μm ($\Xi = 7.5$), (*d*) $a = 70$ μm ($\Xi = 5.83$), (*e*) $a = 50$ μm ($\Xi = 4.17$) and (*f*) $a = 40$ μm ($\Xi = 3.33$), for $f = 100$ kHz. The corresponding acoustic wavelength is $\lambda = 14.45$ mm, while the actual wavelength is 14.14 mm $\geqslant \lambda_R \geqslant$ 12.67 mm. The viscous boundary layer has a thickness of $\delta = 12$ μm. The first velocity node is at $z = 0$, while the first velocity antinode appears at $z = \lambda_R/4$. Arrows indicate the direction of the flow.

We observe that the periodicity of the streaming pattern with respect to the z-axis, and within the first few vortices, is very distinct when only a single type of streaming is present (e.g. in figure 6*a*,*e*,*f*), compared to the situations where Rayleigh and Schlichting streaming vortices coexist (e.g. in figure 6*b*–*d*). The first-order acoustic fields are periodic in z, but their amplitudes are exponential functions of z. Then, at the second order, the time-averaging of the products of first-order fields leads to the decoupling of the sinusoidal

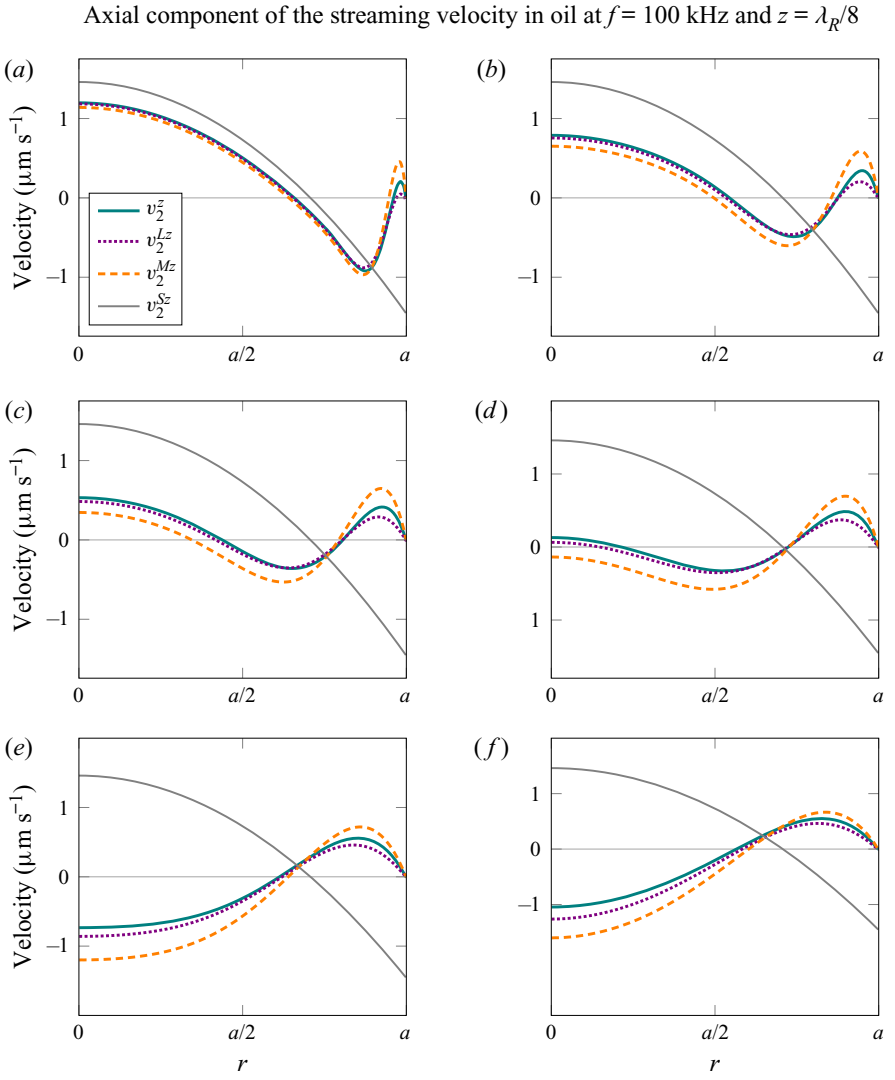

Figure 8. The analysis of the axial velocity profiles in oil, at $z = \lambda_R/8$, for a tube radius of (*a*) $a = 270$ μm ($\Xi = 22.5$), (*b*) $a = 120$ μm ($\Xi = 10$), (*c*) $a = 90$ μm ($\Xi = 7.5$), (*d*) $a = 70$ μm ($\Xi = 5.83$), (*e*) $a = 50$ μm ($\Xi = 4.17$) and (*f*) $a = 40$ μm ($\Xi = 3.33$), for $f = 100$ kHz and $p_a = 100$ kPa. Also shown for comparison are the z-components of the Eulerian streaming velocity, v_2^z, the Lagrangian streaming velocity, v_2^{Lz}, the average mass transport velocity, v_2^{Mz}, and a reference velocity (evaluated at $z = \lambda/8$) from Schuster & Matz (1940), v_2^{Sz}, given as (G1) in appendix G.

and exponential z-dependencies from products into sums. This results in the observed non-periodic behaviour along the z-axis at the second order.

The streaming patterns in figure 6 are plotted for one ideal wavelength (λ) along the z-axis. However, we can observe that the streaming patterns and the actual wavelength (λ_R) shrink along the z-axis with the decrease of Ξ. This follows from the increase of k_R with the decrease of Ξ, which is shown in figure 2.

In figures 8 and 9, we look at the axial and radial velocity profiles, respectively, corresponding to the cases analysed in figures 6 and 7. The superscripts $\square^z$ and $\square^r$ denote

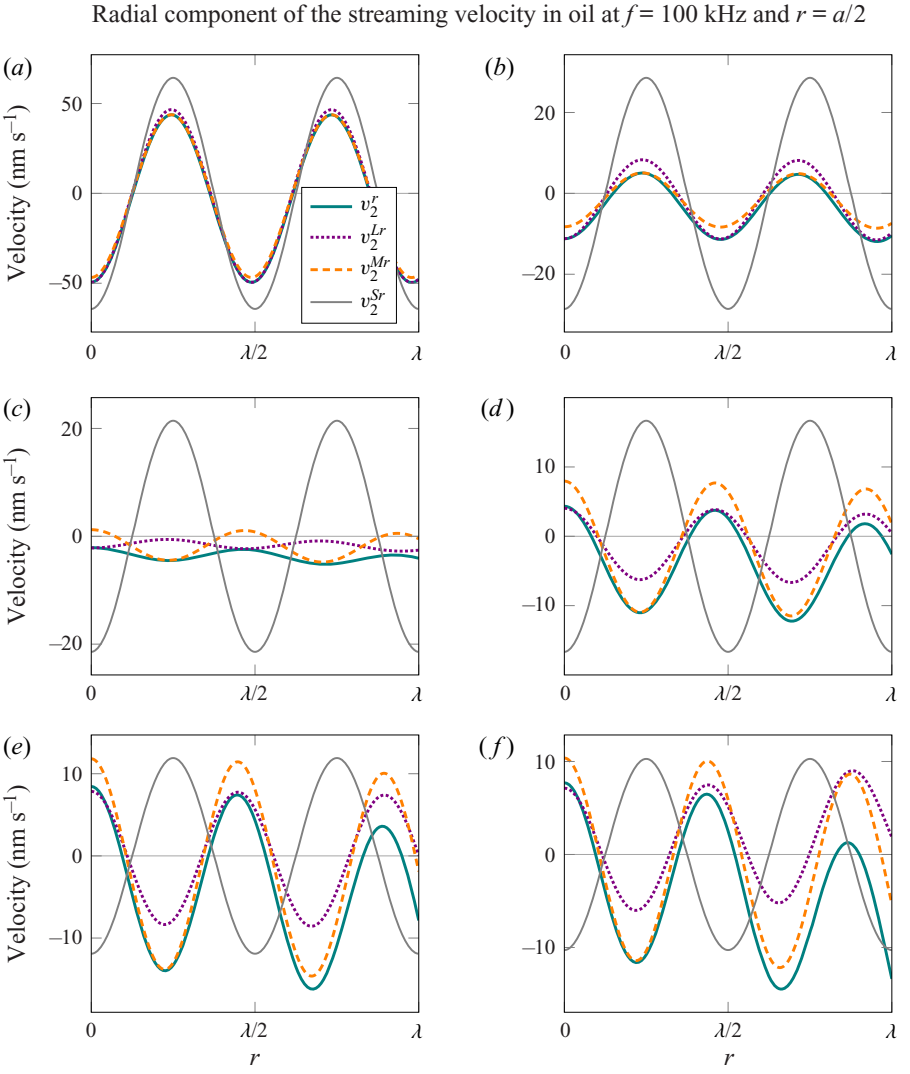

Figure 9. Analysis of the radial velocity profiles in oil, at $r = a/2$, for a tube radius of (*a*) $a = 270$ μm ($\Xi = 22.5$), (*b*) $a = 120$ μm ($\Xi = 10$), (*c*) $a = 90$ μm ($\Xi = 7.5$), (*d*) $a = 70$ μm ($\Xi = 5.83$), (*e*) $a = 50$ μm ($\Xi = 4.17$) and (*f*) $a = 40$ μm ($\Xi = 3.33$), for $f = 100$ kHz and $p_a = 100$ kPa. Also shown for comparison are the *r*-components of the Eulerian streaming velocity, v_2^r, the Lagrangian streaming velocity, v_2^{Lr}, the average mass transport velocity, v_2^{Mr}, and a reference velocity from Schuster & Matz (1940), v_2^{Sr}, given as (G1) in appendix G.

the *z*- and *r*-components of the velocity, respectively (e.g. $v_2^z = \langle \boldsymbol{v}_2 \rangle \cdot \boldsymbol{e}_z$). We analyse profiles of four different velocities: v_2^z and v_2^r relate to the Eulerian streaming velocity $\langle \boldsymbol{v}_2 \rangle$; v_2^{Lz} and v_2^{Lr} relate to the Lagrangian streaming velocity $\langle \boldsymbol{v}_2 \rangle^L$; v_2^{Mz} and v_2^{Mr} relate to the average mass transport velocity $\langle \boldsymbol{v}_2 \rangle^M$; and we also plot v_2^{Sz} and v_2^{Sr}, which correspond to the model by Schuster & Matz (1940), given as (G1) in appendix G. The axial velocity profiles, in figure 8, are plotted through the radius of the tube, at $z = \lambda_R/8$, i.e. at the middle of the first streaming vortex along the *z*-axis, starting from $z = 0$. We observe that the magnitudes of v_2^z, v_2^{Lz} and v_2^{Mz} are largest when one type of streaming vortex is

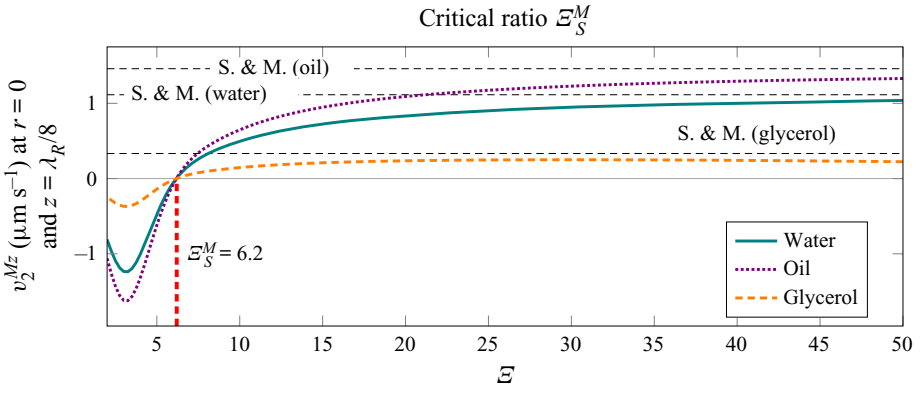

Figure 10. The z-component of the average mass transport velocity, v_2^{Mz}, at $r = 0$ and $z = \lambda_R/8$, depending on the normalized tube radius $\Xi = a/\delta$, for $f = 100$ kHz and $p_a = 100$ kPa. The critical ratio Ξ_S^M is defined as the value of Ξ at which v_2^{Mz} changes direction. The velocity magnitudes (S. & M.) calculated with the model of Schuster & Matz (1940) are given for reference (see (G2) in appendix G).

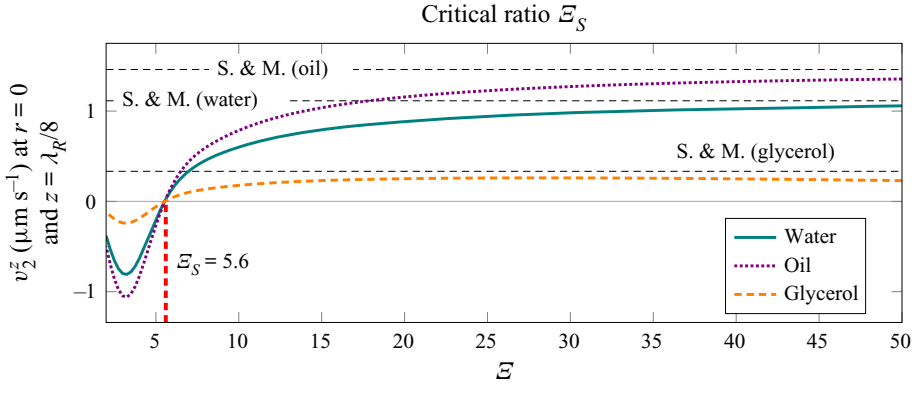

Figure 11. The z-component of the Eulerian streaming velocity, v_2^z, at $r = 0$ and $z = \lambda_R/8$, depending on the normalized tube radius $\Xi = a/\delta$, for $f = 100$ kHz and $p_a = 100$ kPa. The critical ratio Ξ_S is defined as the value of Ξ at which v_2^z changes direction. The velocity magnitudes (S. & M.) calculated with the model of Schuster & Matz (1940) are given for reference (see (G2) in appendix G).

dominant, i.e. at $\Xi = 22.5$ ($a = 270$ μm) and at $\Xi = 3.33$ ($a = 40$ μm). The profiles are, outside the viscous boundary layer, well aligned with v_2^{Sz} at $\Xi = 22.5$, but the difference becomes more and more significant as the ratio Ξ decreases, which is reasonable since Schuster & Matz (1940) assumed $\Xi \gg 1$. After reaching a certain critical ratio Ξ (referred to later as Ξ_S), the change of the direction of the z-component of the streaming velocity at $r = 0$ indicates the qualitative change in the behaviour which is not captured by the model of Schuster & Matz (1940). Namely, the Schlichting streaming vortex spreads throughout the whole radius of the tube, as seen in figure 8(e,f).

The analysis of the critical ratios Ξ_S^M and Ξ_S at $f = 100$ kHz, in figures 10 and 11, shows that the ratios are invariant with respect to the fluid properties, as they are the same for water, oil and glycerol. Figures 10 and 11 show the evolution of the z-components of the Eulerian streaming velocity and average mass transport velocity, respectively, at $r = 0$. Both evaluations are done at $z = \lambda_R/8$, (i.e. the middle of the first streaming vortex along the z-axis). The ratios Ξ_S^M and Ξ_S are defined as the values of Ξ at which the Eulerian

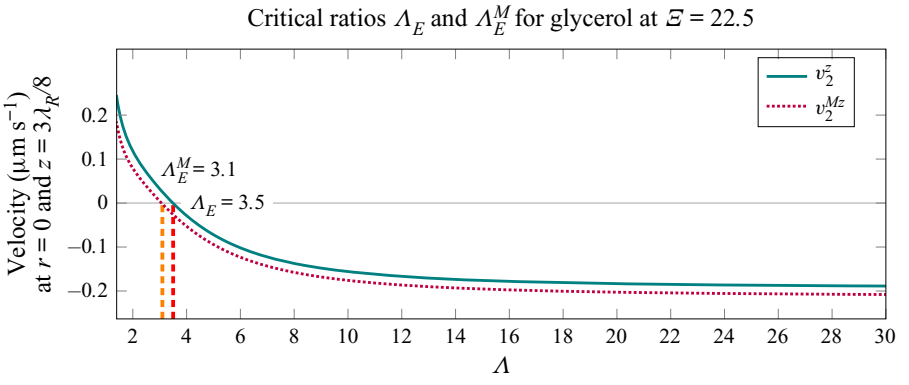

Figure 12. The z-components of the average mass transport velocity and the Eulerian streaming velocity, v_2^{Mz} and v_2^z, respectively, in glycerol. The velocities depend on the normalized acoustic wavelength $\Lambda = \lambda/a$, which is varied by varying the frequency (10.441 MHz $\geq f \geq$ 22.738 kHz) and the radius of the tube (131.4 μm $\leq a \leq$ 2814.6 μm), keeping Ξ constant at 22.5. The velocities are evaluated at $r = 0$ and $z = 3\lambda_R/8$, for $p_a = 100$ kPa. The critical ratios Λ_E^M and Λ_E are defined as the values of Λ at which v_2^{Mz} and v_2^z, respectively, change direction.

streaming velocity and the average mass transport velocity, respectively, in the centre of the tube change sign, as this indicates the disappearance of the Rayleigh streaming. The critical ratios resulting from the discussed analysis are $\Xi_S^M = 6.2$ and $\Xi_S = 5.6$.

In addition, figure 11 shows the values for the streaming velocity magnitude using the model of Schuster & Matz (1940). The equation for the velocity magnitude is given as (G2) in appendix G. We observe that the simplified model (Schuster & Matz 1940) matches well with our solution when the radius of the tube is large relative to the thickness of the viscous boundary layer, i.e. for $\Xi \gg 1$. However, for $\Xi \lesssim 20$ the simplified model (Schuster & Matz 1940) is not valid anymore.

5.3. *Effect of the acoustic wavelength on the streaming*

The analysis of the streaming patterns at higher frequencies and for the same range of Ξ reveals no significant differences in the streaming patterns, assuming $\Lambda = \lambda/a \gg 1$ and consequently $\lambda/\delta \gg 1$. However, for glycerol, the tube radius corresponding to $\Xi = 22.5$ (the largest value of Ξ analysed in figure 6) can approach the wavelength at frequencies that are attainable in microfluidic devices. Keeping Ξ constant at 22.5 and reducing Λ through manipulation of the frequency and radius leads to the change of the z-component of the streaming velocity at $z = 3\lambda_R/8$, as depicted in figure 12. This eventually leads to the change of the direction of the analysed velocity, which signals the appearance of large-scale Eckart-like streaming, at $\Lambda = \Lambda_E$. The critical ratios based on the average mass transport velocity and the Eulerian streaming velocity are $\Lambda_E^M = 3.1$ and $\Lambda_E = 3.5$, respectively. In addition, we observe that the streaming velocity is constant with respect to Λ, for $\Lambda \gtrsim 20$. Additional studies reveal that Λ_E^M and Λ_E are not invariant with respect to Ξ, and increase as Ξ decreases.

The transition from the Rayleigh-plus-Schlichting streaming regime at $\Lambda > \Lambda_E^M$ to the Eckart-plus-Schlichting regime at $\Lambda < \Lambda_E^M$ is also studied through the evolution of the average mass transport velocity patterns in figure 13. The ratio Ξ is kept constant at 22.5, while the ratio Λ is varied through adjustment of the frequency and the radius of the tube. The resulting patterns are qualitatively different from the patterns in oil shown

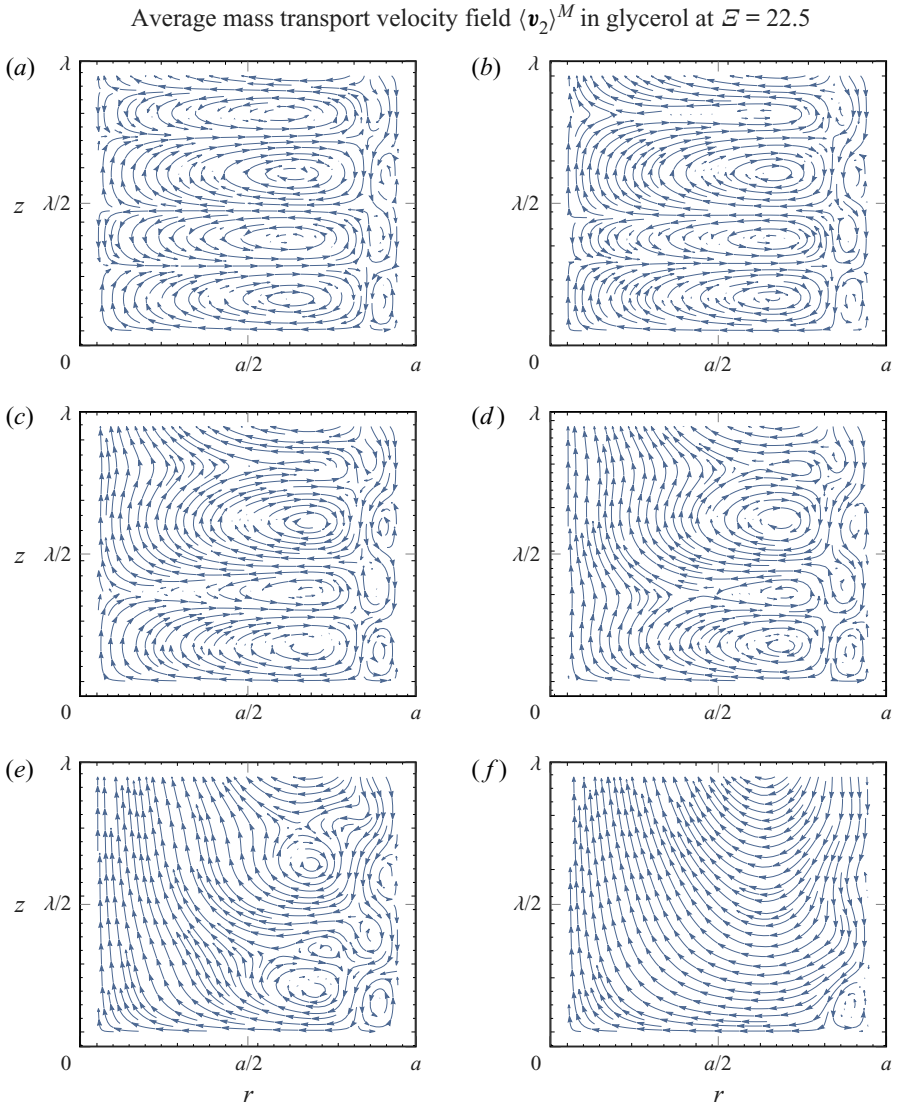

Figure 13. The average mass transport velocity patterns in glycerol, for (*a*) $\Lambda = 10$, (*b*) $\Lambda = 4$, (*c*) $\Lambda = 3$, (*d*) $\Lambda = 2.5$, (*e*) $\Lambda = 2$ and (*f*) $\Lambda = 1$. The patterns depend on the normalized acoustic wavelength $\Lambda = \lambda/a$, which is varied by varying the frequency (204.644 kHz $\leq f \leq$ 20.464 MHz) and the radius of the tube (938.2 μm $\geq a \geq$ 93.8 μm), keeping Ξ constant at 22.5. The first velocity node is at $z = 0$, while the first velocity antinode appears at $z = \lambda_R/4$. Arrows indicate the direction of the flow.

in figure 6. The difference is minute for the moderately small Λ of 10 in figure 13(*a*), and becomes very prominent as Λ is decreased all the way to $\Lambda = 1$ in figure 13(*f*), where the Eckart-like streaming dominates near the axis, in addition to small Schlichting vortices near the wall. The large-scale nature of the Eckart-like streaming is further demonstrated in figure 14, where the interval of the analysis is increased from $0 \leq z \leq \lambda$ to $0 \leq z \leq 4\lambda$.

The streaming patterns at $\Lambda < \Lambda_E^M$, e.g. figure 13(*f*), reveal that the streaming flow at the axis of the tube is directed towards the incoming decaying travelling wave and in the opposite direction near the wall. This behaviour is in agreement with the flow in the case

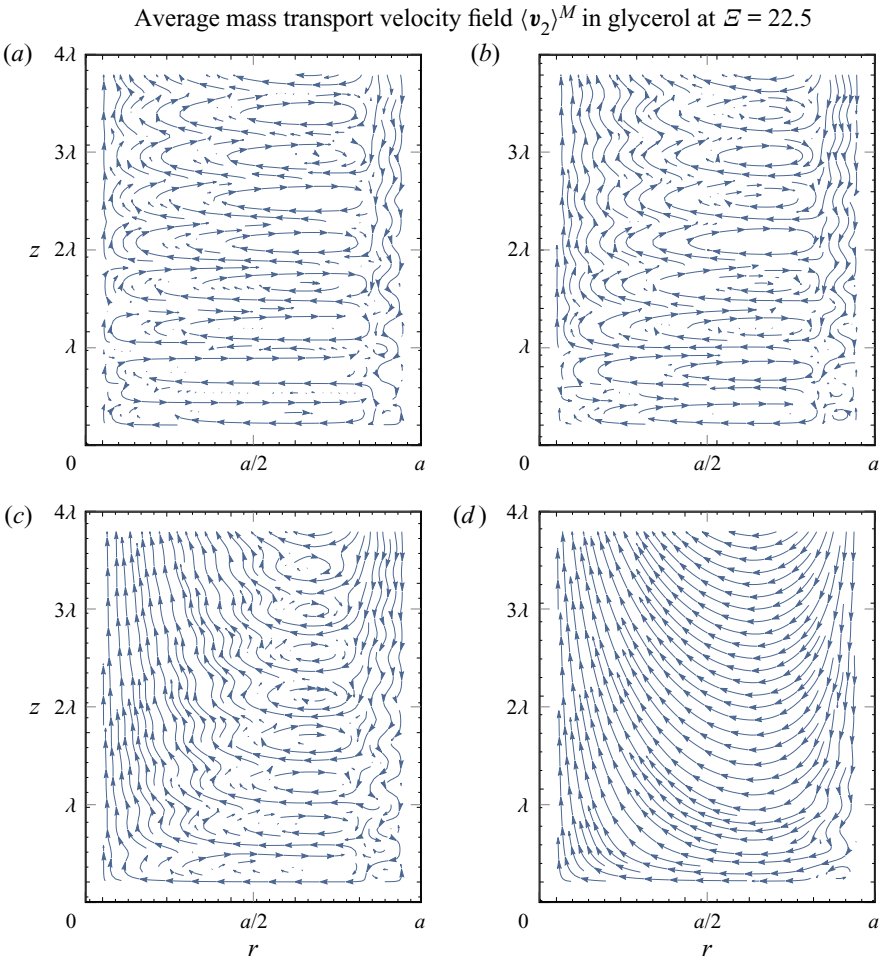

Figure 14. The average mass transport velocity patterns in glycerol, for (*a*) $\Lambda = 10$, (*b*) $\Lambda = 4$, (*c*) $\Lambda = 2.5$ and (*d*) $\Lambda = 1$. The patterns depend on the normalized acoustic wavelength $\Lambda = \lambda/a$, which is varied by varying the frequency (204.644 kHz $\leq f \leq$ 20.464 MHz) and the radius of the tube (938.2 μm $\geq a \geq$ 93.8 μm), keeping Ξ constant at 22.5. The first velocity node is at $z = 0$, while the first velocity antinode appears at $z = \lambda_R/4$. The patterns are plotted on the interval $0 \leq z \leq 4\lambda$ to reveal the large-scale nature of the streaming flow. Arrows indicate the direction of the flow.

of a travelling wave which grazes the wall (Nyborg 1965, p. 274). Since the acoustic wave propagates through the whole cross-section of the tube, the described behaviour differs from the regular Eckart streaming (Eckart 1948), where the acoustic source is smaller than the tube cross-section.

5.4. *Contribution of the compressibility of the streaming flow*

Streaming flow is sometimes assumed incompressible in similar situations (e.g. Schuster & Matz 1940; Doinikov *et al.* 2017), which means that the second-order continuity equation (4.1), namely $\nabla \cdot \langle \boldsymbol{v}_2 \rangle = -1/\rho_0 \nabla \cdot \langle \rho_1 \boldsymbol{v}_1 \rangle$, is simplified to $\nabla \cdot \langle \boldsymbol{v}_2 \rangle = 0$. Nevertheless, the validity of this assumption is not clear, and the effect of compressibility at the second order, as remarked by Menguy & Gilbert (2000), still poses one of the main unresolved issues in the field of acoustic streaming.

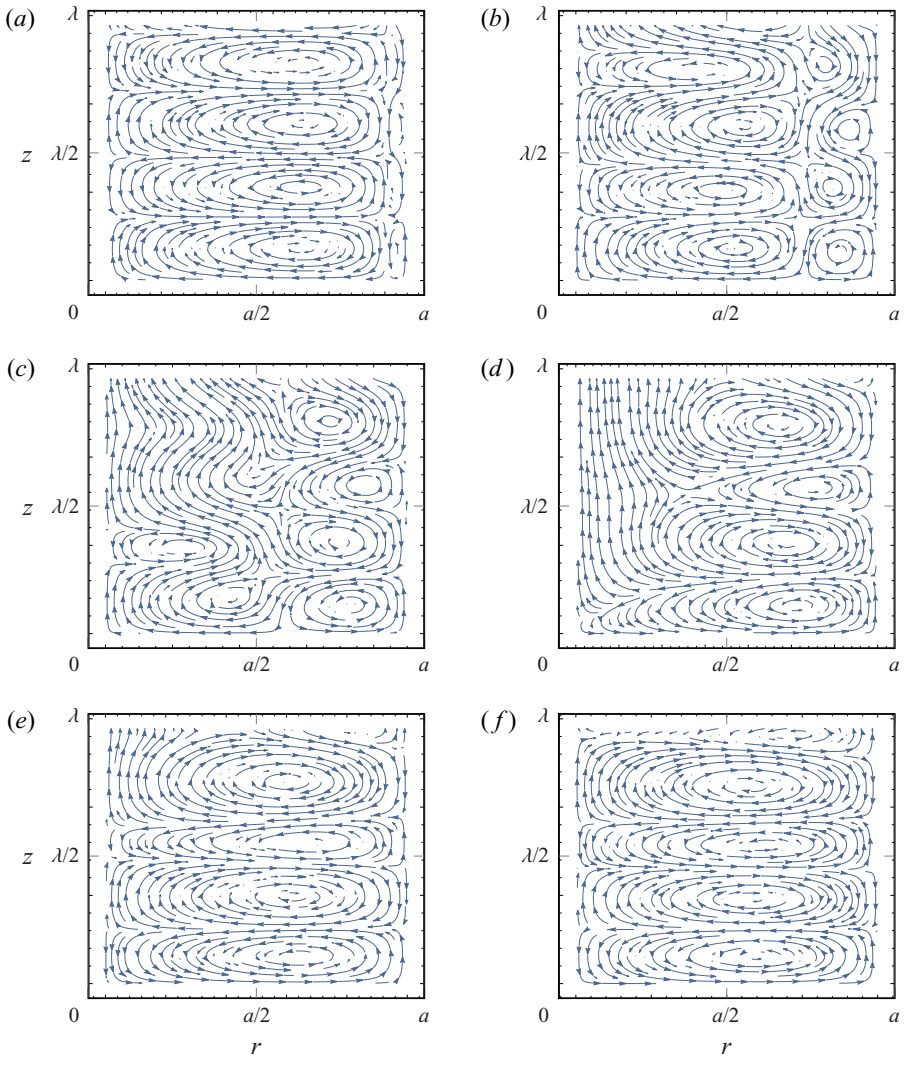

Figure 15. The Eulerian streaming velocity patterns in oil, using the Eulerian divergence-free formulation, i.e. $\boldsymbol{\nabla} \cdot \langle \boldsymbol{v}_2 \rangle = 0$, for a tube radius of (*a*) $a = 270$ μm ($\Xi = 22.5$), (*b*) $a = 120$ μm ($\Xi = 10$), (*c*) $a = 90$ μm ($\Xi = 7.5$), (*d*) $a = 70$ μm ($\Xi = 5.83$), (*e*) $a = 50$ μm ($\Xi = 4.17$) and (*f*) $a = 40$ μm ($\Xi = 3.33$), for $f = 100$ kHz. The corresponding acoustic wavelength is $\lambda = 14.45$ mm, while the actual wavelength is $14.14 \text{ mm} \geqslant \lambda_R \geqslant 12.67$ mm. The viscous boundary layer has a thickness of $\delta = 12$ μm. The first velocity node is at $z = 0$, while the first velocity antinode appears at $z = \lambda_R/4$. Arrows indicate the direction of the flow.

Here, we use the solution for $\langle \boldsymbol{v}_2 \rangle$ that results if the aforementioned continuity equation (4.1) is replaced by $\boldsymbol{\nabla} \cdot \langle \boldsymbol{v}_2 \rangle = 0$ (this renders the irrotational part of the streaming velocity, namely $\boldsymbol{\nabla}\varphi_2$, zero, and changes the remaining constants C_1 and C_3).

Since the concept of the average mass transport velocity does not arise naturally in this case, i.e. it is not divergence-free by definition, we plot only the Eulerian streaming velocity patterns, in figure 15. Comparison with figures 6 and 7 shows that the incompressible Eulerian streaming velocity patterns in figure 15 better resemble

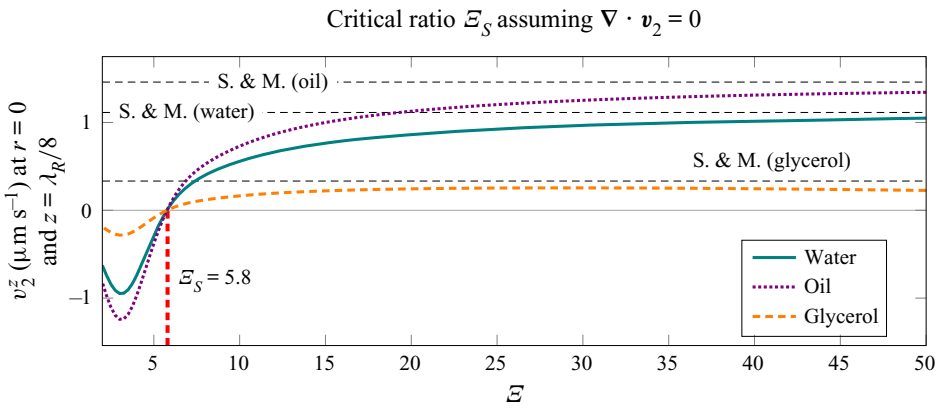

Figure 16. The z-component of the Eulerian streaming velocity, v_2^z, using the divergence-free formulation, i.e. $\nabla \cdot \langle \boldsymbol{v}_2 \rangle = 0$, at $r = 0$ and $z = \lambda_R/8$, depending on the normalized tube radius $\Xi = a/\delta$, for $f = 100$ kHz and $p_a = 100$ kPa. The critical ratio Ξ_S is defined as the value of Ξ at which v_2^z changes direction. The velocity magnitudes (S. & M.) calculated with the model of Schuster & Matz (1940) are given for reference (see (G2) in appendix G).

the average mass transport velocity patterns from figure 6 than the corresponding Eulerian streaming velocity patterns from figure 7. Additionally, in the transition phase, when Rayleigh streaming is gradually disappearing (figure 15*b–d*), the incompressible patterns preserve the periodicity with respect to the z-axis better than the patterns of the compressible solution.

With the modified solution for the incompressible streaming flow, we analyse the critical ratio Ξ_S. The results, in figure 16, indicate that the compressibility slightly decreases Ξ_S, as the incompressible solution yields $\Xi_S = 5.8$, compared to the value $\Xi_S = 5.6$ of the compressible solution (figure 11).

5.5. *Contribution of individual streaming source terms*

We repeat the average mass transport velocity pattern analysis from figure 6, but this time we set $E_R(r) = E_I(r) = 0$, i.e. we omit the usually neglected source term in the streaming equations (4.2) (see e.g. Rayleigh 1884; Schlichting 1932; Lighthill 1978; Doinikov *et al.* 2017). The simplified solution gives the results shown in figure 17. We observe that the average mass transport velocity patterns differ from those given in figure 6 for the (compressible) average mass transport velocity patterns. Furthermore, the patterns closely resemble the incompressible Eulerian streaming velocity patterns from figure 15.

In figure 18, we analogously repeat the analysis of Ξ_S^M from figure 11. We observe that the transition from the Rayleigh-plus-Schlichting streaming to the Schlichting streaming occurs at lower value of Ξ when the source terms $E_R(r)$ and $E_I(r)$ are neglected. Specifically, the critical normalized radius Ξ_S^M is reduced from 6.2 to 5.8. Interestingly, this value corresponds to the Eulerian-streaming-velocity-based Ξ_S of the incompressible streaming flow solution (figure 15).

6. Conclusions

We derived an analytical solution for the motion of a viscous fluid at the first and at the second order in a tube of infinite length containing a pseudo-standing wave composed of two counterpropagating decaying travelling waves along the axis of the tube. The solution

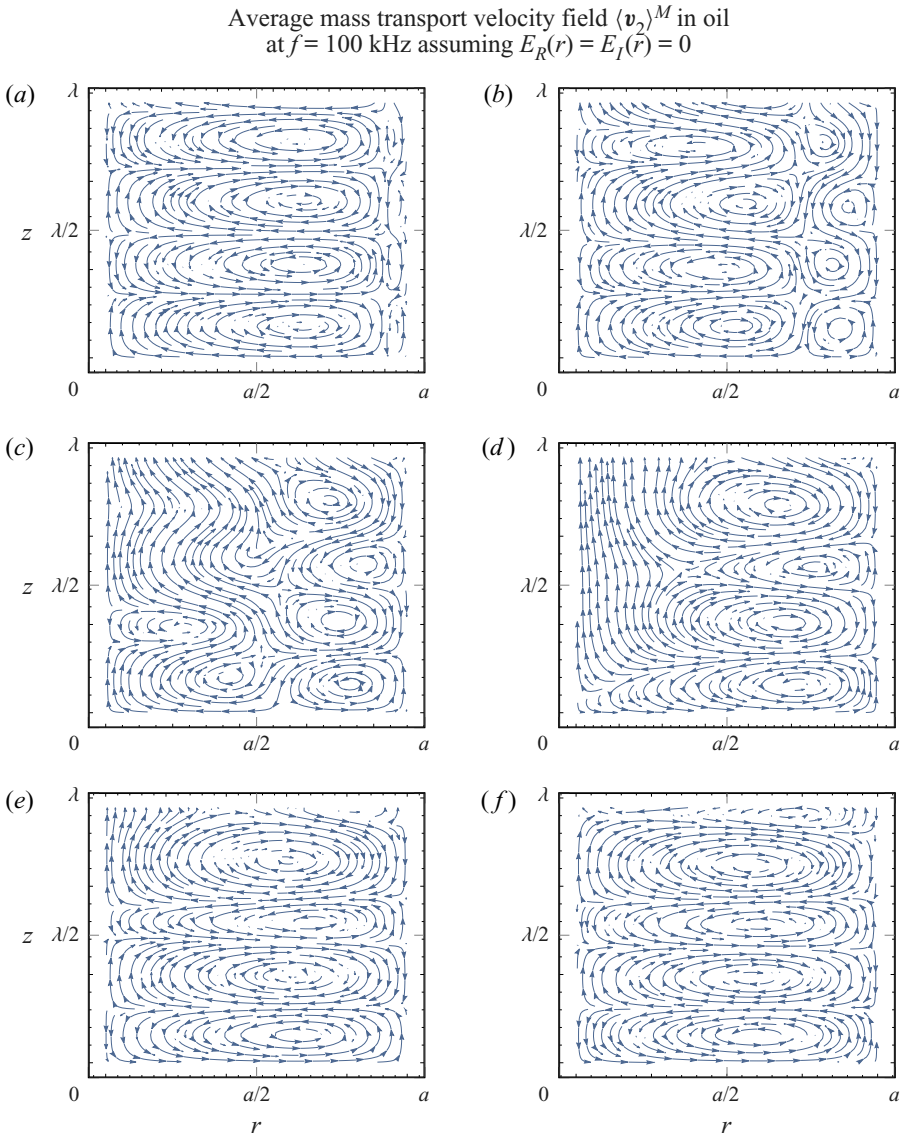

Figure 17. The average mass transport velocity patterns in oil, assuming $E_R(r) = E_I(r) = 0$, for a tube radius of (*a*) $a = 270$ μm ($\Xi = 22.5$), (*b*) $a = 120$ μm ($\Xi = 10$), (*c*) $a = 90$ μm ($\Xi = 7.5$), (*d*) $a = 70$ μm ($\Xi = 5.83$), (*e*) $a = 50$ μm ($\Xi = 4.17$) and (*f*) $a = 40$ μm ($\Xi = 3.33$), for $f = 100$ kHz. The corresponding acoustic wavelength is $\lambda = 14.45$ mm, while the actual wavelength is 14.14 mm $\geqslant \lambda_R \geqslant$ 12.67 mm. The viscous boundary layer has a thickness of $\delta = 12$ μm. The first velocity node is at $z = 0$, while the first velocity antinode appears at $z = \lambda_R/4$. Arrows indicate the direction of the flow.

is valid for arbitrary thicknesses of the viscous boundary layer δ relative to the radius of the tube a, and is not restricted by the acoustic wavelength λ. In addition, the applicability of our solution was demonstrated through analysis of several cases, with the help of numerical integration in Mathematica 12.0 (Wolfram Research, Inc., 2019), revealing the streaming patterns and their evolution with respect to the varying problem parameters. The Mathematica Notebook file with the implementations of all necessary expressions

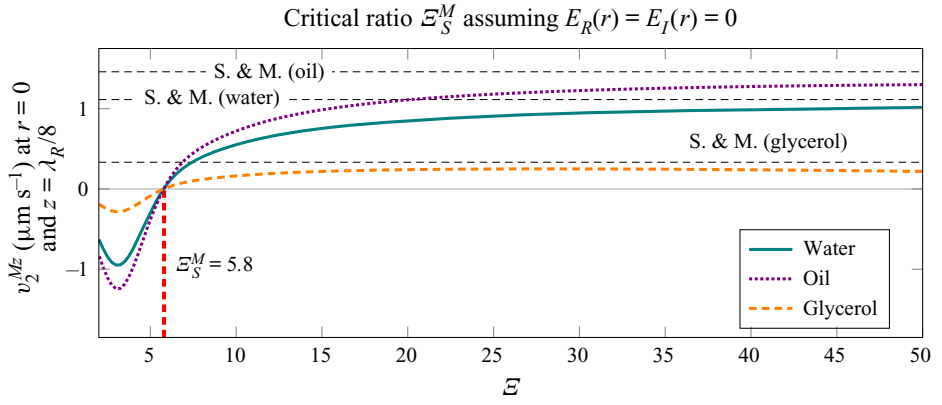

Figure 18. The z-component of the average mass transport velocity, v_2^{Mz}, assuming $E_R(r) = E_I(r) = 0$, at $r = 0$ and $z = \lambda_R/8$, depending on the normalized tube radius $\Xi = a/\delta$, for $f = 100$ kHz and $p_a = 100$ kPa. The critical ratio Ξ_S^M is defined as the value of Ξ at which v_2^{Mz} changes direction. The velocity magnitudes (S. & M.) calculated with the model of Schuster & Matz (1940) are given for reference (see (G2) in appendix G).

for evaluation of arbitrary streaming fields is available in the supplementary material. In our analysis, we observed two types of streaming vortices, namely Rayleigh streaming (fluid flow from the velocity node to the antinode near the axis of the tube) and the oppositely directed Schlichting streaming. The Rayleigh streaming is suppressed by the Schlichting streaming when the ratio of the tube radius to the thickness of the viscous boundary layer (i.e. $\Xi = a/\delta$) is below the critical value of $\Xi_S^M = 6.2$, considering the average mass transport velocity, for $\Lambda = \lambda/a \gg 1$. If the Eulerian streaming velocity is considered, the transition occurs at $\Xi_S = 5.6$. The critical radii Ξ_S^M and Ξ_S at which the transitions between different streaming regimes occur are invariant with respect to the material parameters, as long as we are in the limit of $\Lambda \gg 1$. Similar behaviour was also predicted for a two-dimensional channel by Hamilton *et al.* (2003*a*), who evaluated Ξ_S^M at 5.7, but with the radius replaced by the half-width of their channel.

The vortices appear to be very distinct when a single vortex type, either Rayleigh or Schlichting, is dominant, e.g. figure 6(*a*,*f*). In the intermediate region, where Ξ is decreasing towards Ξ_S, we observe non-periodic behaviour along the z-axis (e.g. figure 6*c*,*d*), which can be attributed to the decaying nature of the pseudo-standing wave. The amplitude of the acoustic streaming was found to be dependent on the normalized radius Ξ. The amplitude is lowest when Ξ corresponds to the regime where neither Rayleigh nor Schlichting streaming dominates (i.e. $20 \gtrsim \Xi > \Xi_S$). However, for $\Xi \gtrsim 20$, the streaming velocity magnitude at the centre of the tube matches relatively well to the solution of Schuster & Matz (1940).

When $\Xi > \Xi_S$, decreasing Λ can result in a transition from Rayleigh streaming vortices to a large-scale Eckart-like streaming (figure 13). The critical ratio Λ at which this transition occurs was evaluated for the case of glycerol at a constant Ξ of 22.5, and stands at $\Lambda_E^M = 3.5$ for the average mass transport velocity, and at $\Xi_E = 3.1$ for the Eulerian streaming velocity (figure 12).

The investigation of the contribution of the compressibility of the streaming flow indicated that the resulting Eulerian streaming velocity patterns (figure 15) better resemble the average mass transport velocity patterns of the compressible solution (figure 6) than the patterns of the compressible Eulerian streaming velocity (figure 7).

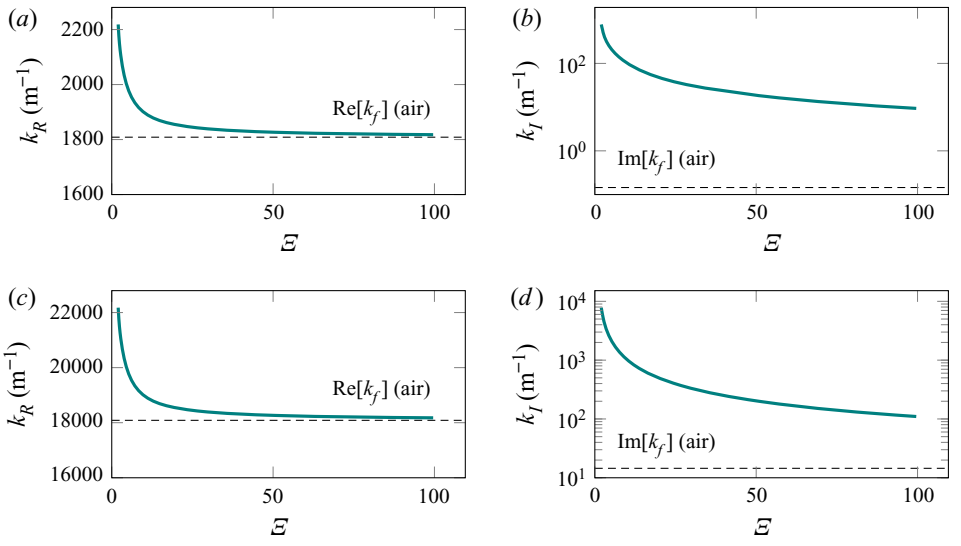

Figure 19. The real and imaginary parts of the wavenumber in air according to (3.31) and (3.32), respectively: (*a*) k_R at $f = 100$ MHz; (*b*) k_I at $f = 100$ kHz; (*c*) k_R at $f = 1$ MHz; (*d*) k_I at $f = 1$ MHz. The dimensionless ratio $\Xi = a/\delta$ represents the varying tube radius relative to the viscous boundary layer thickness. The real and imaginary parts of the wavenumber in an unbounded fluid domain k_f are plotted for reference.

Compressibility appears to decrease the critical ratio Ξ_S, since the incompressible solution yields $\Xi_S = 5.8$, whereas the compressible solution yields $\Xi_S = 5.6$.

The analysis of the effects of the individual streaming source terms revealed that all terms originating from the spatial variation of the Reynolds stress have to be considered to correctly predict the streaming patterns. Neglecting the commonly-neglected the source term, namely $\langle \boldsymbol{v}_1 \boldsymbol{\nabla} \cdot \boldsymbol{v}_1 \rangle = 0$ (for example, Rayleigh (1884), Schlichting (1932), Lighthill (1978) and Doinikov *et al.* (2017) neglect this term), leads to the decrease of the critical ratio Ξ_S^M (from 6.2 to 5.8), but still offers a good approximation. Interestingly, the average-mass-transport-velocity-based $\Xi_S^M = 5.8$ of the solution with partially neglected source terms matches the Eulerian-streaming-velocity-based Ξ_S of the incompressible solution, and the corresponding streaming patterns match as well.

Supplementary material. Supplementary material is available at https://doi.org/10.1017/jfm.2020.1046.

Acknowledgements. We would like to express our gratitude to A. A. Doinikov for helpful discussions on the topics involving acoustic streaming that served as an inspiration for the present work.

Declaration of interests. The authors report no conflict of interest.

Author ORCIDs.
Alen Pavlic https://orcid.org/0000-0002-3260-4090;
Jürg Dual https://orcid.org/0000-0001-5861-9058.

Appendix A

This appendix contains the results for air (material properties are given in table 1). The wavenumber in air for $f = 100$ kHz and $f = 1$ MHz is given in figure 19. The first-order pressure for air at different tube radii is given in figure 20. In figure 21, it is shown that the discovered critical ratios $\Xi_S = 5.6$ and $\Xi_S^M = 6.2$, in the limit of $\lambda \gg a$, also hold for air.

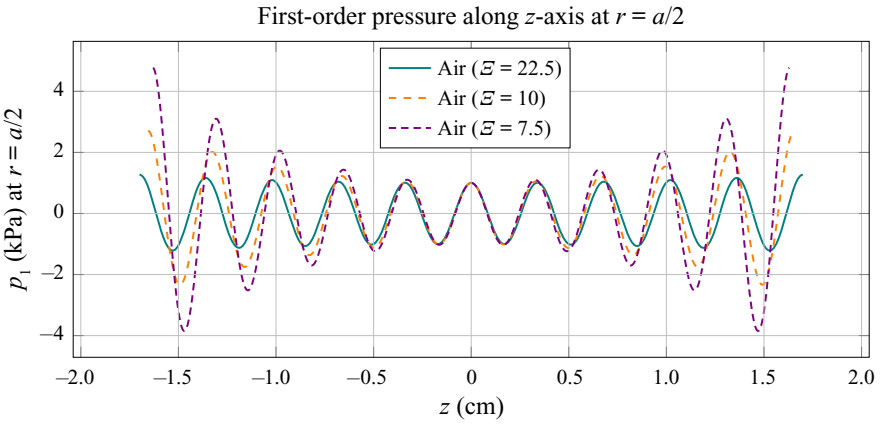

Figure 20. The first-order pressure in air along the z-axis, at $r = a/2$, for $f = 100$ kHz and $p_a = 1$ kPa. The dimensionless ratio $\Xi = a/\delta$ represents the varying tube radius relative to the viscous boundary layer thickness of $\delta = 7.13$ µm. For each radius of the tube, we plot the pressure in the range of $-5\lambda_R < z < 5\lambda_R$, with $\lambda_R = 2\pi/k_R$.

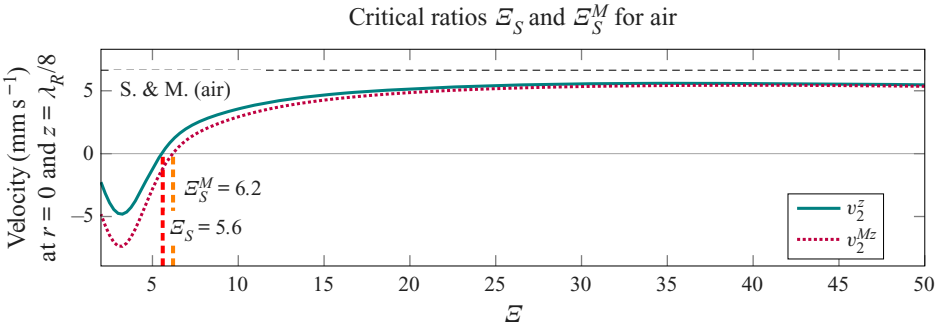

Figure 21. The z-components of the Eulerian streaming velocity, v_2^z, and of the average mass transport velocity, v_2^{Mz}, in air, at $r = 0$ and $z = \lambda_R/8$, depending on the normalized tube radius $\Xi = a/\delta$, for $f = 100$ kHz and $p_a = 1$ kPa. The critical ratios Ξ_S and Ξ_S^M are defined as the values of Ξ at which v_2^z and v_2^{Mz}, respectively, change direction. The velocity magnitude (S. & M.) calculated with the model of Schuster & Matz (1940) is given for reference (see (G2) in appendix G).

Appendix B

Here we analyse the convergence of different parts of the solution with respect to the summation limit i_{max}, at which the infinite summations in (4.26), (4.27), (4.56), (4.57), (E1) and (E2) are truncated. In figure 22, the convergence of the z-component of the Eulerian streaming velocity, v_2^z, is evaluated at different positions (figure 22*e–h*), in addition to the convergence of the constants C_1 and C_3 (figure 22*a–d*). The exemplary convergence study in figure 22 corresponds to the case from figure 6(*f*), with oil at 100 kHz, $p_a = 100$ kPa, $a = 40$ µm and $\Xi = 3.33$. The solution appears to be converged for $i_{max} \gtrsim 100$. However, it appears from figure 22(*e*) that v_2^z converges slower when the point of evaluation is closer to $r = a$. This has been confirmed by further analysis of convergence at higher Ξ, where the sufficient i_{max} was evaluated to be much higher. For the purposes of our study, using i_{max} of up to 200 was sufficient.

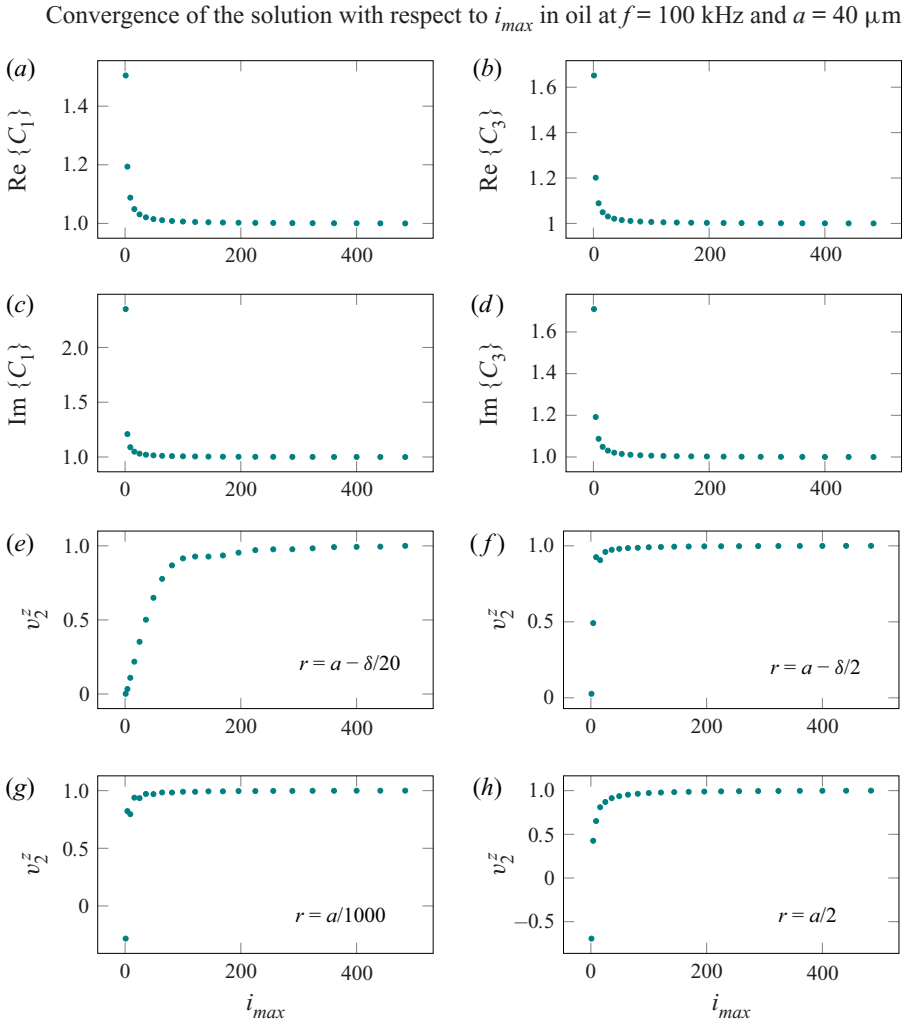

Figure 22. Analysis of the convergence of different parts of the solution with respect to the summation index i_{max}, at which the infinite summations in (4.26), (4.27), (4.56), (4.57), (E1) and (E2) are truncated. Panels (*a–d*) show the convergence of the constants C_1 and C_3, and panels (*e–h*) the convergence of the z-component of the Eulerian streaming velocity, v_2^z, evaluated at different positions along $a/1000 \leq r \leq a - \delta/20$. The values of each quantity are normalized with the value at the maximal i_{max} in the convergence study. (*a*) Re $\{C_1\}$. (*b*) Re $\{C_3\}$. (*c*) Im $\{C_1\}$. (*d*) Im $\{C_3\}$. (*e–h*) v_2^z at the r-values indicated.

Appendix C

Here we give the expressions for the functions $R_R(r)$, $E_R(r)$, $R_I(r)$ and $E_I(r)$:

$$R_R(r) = \frac{-A_1}{r|k|^2|J_1(q_v a)|^2}\left(rkq_f A_1^*\left[J_0(q_f r)J_1(q_v a)k^2 + q_f q_v J_0(q_v r)J_1(q_f a)\right]^*\right.$$
$$\left[|k|^2 J_1(q_v a)J_1(q_f r) - J_1(q_f a)\left(2kk_R + q_v^2\right)J_1(q_v r)\right]$$
$$\left.-rk\left[k^2 J_1(q_v a)J_0(q_f r) + q_f q_v J_1(q_f a)J_0(q_v r)\right]\right.$$

$$\left[q_f A_1\left(J_1(q_v a)J_1(q_f r)k^2+q_v^2 J_1(q_f a)J_1(q_v r)\right)\right]^*$$
$$+q_f k^*\left\{k_v^2 J_1(q_f a)\left(J_1(q_v r)-rq_v J_0(q_v r)\right)\right.$$
$$\left(q_f A_1\left[J_1(q_v a)J_1(q_f r)-J_1(q_f a)J_1(q_v r)\right]\right)^*$$
$$\left(k^2 J_1(q_v a)J_1(q_f r)+q_v^2 J_1(q_f a)J_1(q_v r)\right)$$
$$\left(q_f A_1\left[rq_v J_0(q_v r)J_1(q_f a)-J_1(q_v r)J_1(q_f a)+J_1(q_v a)\left(J_1(q_f r)-rq_f J_0(q_f r)\right)\right]\right)^*$$
$$+k\left(-rq_v J_1(q_f a)J_0(q_v r)+J_1(q_f a)J_1(q_v r)+J_1(q_v a)\left[rq_f J_0(q_f r)-J_1(q_f r)\right]\right)$$
$$\left.\left(kq_f A_1\left[J_1(q_v a)J_1(q_f r)-J_1(q_f a)J_1(q_v r)\right]\right)^*\right\}, \tag{C1}$$

$$R_I(r)=\frac{-A_1}{r|k|^2|J_1(q_v a)|^2}\left(rkq_f A_1^*\left[J_0(q_f r)J_1(q_v a)k^2+q_f q_v J_0(q_v r)J_1(q_f a)\right]^*\right.$$
$$\left[|k|^2 J_1(q_v a)J_1(q_f r)+J_1(q_f a)\left(2\mathrm{i}kk_I+q_v^2\right)J_1(q_v r)\right]$$
$$+rk\left[k^2 J_1(q_v a)J_0(q_f r)+q_f q_v J_1(q_f a)J_0(q_v r)\right]$$
$$\left[q_f A_1\left(J_1(q_v a)J_1(q_f r)k^2+q_v^2 J_1(q_f a)J_1(q_v r)\right)\right]^*$$
$$+q_f k^*\left\{k_v^2 J_1(q_f a)\left(J_1(q_v r)-rq_v J_0(q_v r)\right)\right.$$
$$\left(q_f A_1\left[J_1(q_v a)J_1(q_f r)-J_1(q_f a)J_1(q_v r)\right]\right)^*$$
$$\left(k^2 J_1(q_v a)J_1(q_f r)+q_v^2 J_1(q_f a)J_1(q_v r)\right)$$
$$\left(q_f A_1\left[rq_v J_0(q_v r)J_1(q_f a)-J_1(q_v r)J_1(q_f a)+J_1(q_v a)\left(J_1(q_f r)-rq_f J_0(q_f r)\right)\right]\right)^*$$
$$+k\left(rq_v J_1(q_f a)J_0(q_v r)-J_1(q_f a)J_1(q_v r)+J_1(q_v a)\left[-rq_f J_0(q_f r)+J_1(q_f r)\right]\right)$$
$$\left.\left(kq_f A_1\left[J_1(q_v a)J_1(q_f r)-J_1(q_f a)J_1(q_v r)\right]\right)^*\right\}, \tag{C2}$$

$$E_R(r)=\frac{A_1}{r^2|k|^2|J_1(q_v a)|^2}\left(k^*\left\{\left(k^2 J_1(q_v a)J_0(q_f r)\left[1-r^2k_f^2\right]+rk^2 q_f J_1(q_v a)J_1(q_f r)\right.\right.\right.$$
$$\left.+rq_f q_v^2 J_1(q_f a)J_1(q_v r)+q_f q_v J_1(q_f a)J_0(q_v r)\right)$$
$$\left(A_1 q_f\left[J_1(q_v a)J_1(q_f r)-J_1(q_f a)J_1(q_v r)\right]\right)^*-r^2 kk_f J_1(q_v a)J_0(q_f r)$$
$$\left(A_1 kq_f\left[J_1(q_v a)J_1(q_f r)-J_1(q_f a)J_1(q_v r)\right]\right)^*$$
$$+\left(k^2 J_1(q_v a)J_0(q_f r)+q_v q_f J_1(q_f a)J_0(q_v r)\right)$$
$$\left.\left(A_1 q_f\left[rq_v J_0(q_v r)J_1(q_f a)-J_1(q_v r)J_1(q_f a)+J_1(q_v a)\left(J_1(q_f r)-rq_f J_0(q_f r)\right)\right]\right)^*\right\}$$
$$+rk\left[rk_f^2 J_1(q_v a)J_0(q_f r)-q_f J_1(q_v a)J_1(q_f r)+q_f J_1(q_f a)J_1(q_v r)\right]$$
$$\left[A_1 q_f\left(k^2 J_1(q_v a)J_1(q_f r)+q_v^2 J_1(q_f a)J_1(q_v r)\right)\right]^*$$

$$+rkq_f\left[J_1(q_v a)\left(rk_f^2 J_1(q_f r)-q_f J_2(q_f r)\right)+q_v J_1(q_f a)J_2(q_v r)\right]$$
$$\left[A_1 k^2 J_0(q_f r)J_1(q_v a)+A_1 q_f q_v J_0(q_v r)J_1(q_f r)\right]^*\Big), \tag{C3}$$

$$E_I(r)=\frac{A_1}{r^2|k|^2|J_1(q_v a)|^2}\Big(k^*\Big\{\Big(k^2 J_1(q_v a)J_0(q_f r)\left[1-r^2k_f^2\right]+rk^2 q_f J_1(q_v a)J_1(q_f r)$$
$$+rq_f q_v^2 J_1(q_f a)J_1(q_v r)+q_f q_v J_1(q_f a)J_0(q_v r)\Big)$$
$$\left(A_1 q_f\left[J_1(q_v a)J_1(q_f r)-J_1(q_f a)J_1(q_v r)\right]\right)^*+r^2 k k_f J_1(q_v a)J_0(q_f r)$$
$$\left(A_1 k q_f\left[J_1(q_v a)J_1(q_f r)-J_1(q_f a)J_1(q_v r)\right]\right)^*$$
$$+\Big(k^2 J_1(q_v a)J_0(q_f r)+q_v q_f J_1(q_f a)J_0(q_v r)\Big)$$
$$\left(A_1 q_f\left[rq_v J_0(q_v r)J_1(q_f a)-J_1(q_v r)J_1(q_f a)+J_1(q_v a)\left(J_1(q_f r)-rq_f J_0(q_f r)\right)\right]\right)^*\Big\}$$
$$-rk\left[rk_f^2 J_1(q_v a)J_0(q_f r)-q_f J_1(q_v a)J_1(q_f r)+q_f J_1(q_f a)J_1(q_v r)\right]$$
$$\left[A_1 q_f\left(k^2 J_1(q_v a)J_1(q_f r)+q_v^2 J_1(q_f a)J_1(q_v r)\right)\right]^*$$
$$-rkq_f\left[J_1(q_v a)\left(rk_f^2 J_1(q_f r)-q_f J_2(q_f r)\right)+q_v J_1(q_f a)J_2(q_v r)\right]$$
$$\left[A_1 k^2 J_0(q_f r)J_1(q_v a)+A_1 q_f q_v J_0(q_v r)J_1(q_f r)\right]^*\Big). \tag{C4}$$

Appendix D

The source terms connected to the scalar velocity potential φ_2 are given below:

$$M_R(r)=-A_1 k_f^2 J_0(q_f^* r)J_0(q_f r)+A_1 q_f^* q_f J_1(q_f^* r)J_1(q_f r)$$
$$+\mathrm{i}B_1 k q_f^* J_1(q_f^* r)J_1(q_v r)-A_1 k^* k J_0(q_f^* r)J_0(q_f r)$$
$$+\mathrm{i}B_1 k^* q_v J_0(q_f^* r)J_0(q_v r), \tag{D1}$$

$$M_I(r)=-A_1 k_f^2 J_0(q_f^* r)J_0(q_f r)+A_1 q_f^* q_f J_1(q_f^* r)J_1(q_f r)$$
$$+\mathrm{i}B_1 k q_f^* J_1(q_f^* r)J_1(q_v r)+A_1 k^* k J_0(q_f^* r)J_0(q_f r)$$
$$-\mathrm{i}B_1 k^* q_v J_0(q_f^* r)J_0(q_v r). \tag{D2}$$

Appendix E

The differentiation of (4.26) with respect to r leads to

$$\frac{\mathrm{d}S_R(r)}{\mathrm{d}r}=\frac{2}{a^2}\sum_{i=1}^{\infty}\frac{\frac{1}{r}J_1(\xi_i r)-\xi_i J_2(\xi_i r)}{[J_2(\xi_i a)]^2\left(\xi_i^2+4k_R^2\right)^2}\Big[\bar{R}_R(\xi_i)+\bar{E}_R(\xi_i)$$
$$-a\xi_i C_1 J_2(\xi_i a)+a\xi_i C_2\left(\xi_i^2 J_2(\xi_i a)-8k_R^2\right)\Big], \tag{E1}$$

and similarly for (4.27),

$$\frac{\mathrm{d}S_I(r)}{\mathrm{d}r} = \frac{2}{a^2}\sum_{i=1}^{\infty}\frac{\frac{1}{r}J_1(\xi_i r) - \xi_i J_2(\xi_i r)}{[J_2(\xi_i a)]^2\left(\xi_i^2 - 4k_I^2\right)^2}\Big[\bar{R}_I(\xi_i) + \bar{E}_I(\xi_i) \\ -a\xi_i C_3 J_2(\xi_i a) + a\xi_i C_4\left(\xi_i^2 J_2(\xi_i a) + 8k_I^2\right)\Big]. \tag{E2}$$

The differentiation of (4.41) with respect to r leads to

$$\frac{\mathrm{d}U_R(r)}{\mathrm{d}r} = \pi \mathrm{i}k_R J_1(2\mathrm{i}k_R r)\int_0^r xM_R(x)Y_0(-2\mathrm{i}k_R x)\,\mathrm{d}x \\ + \pi \mathrm{i}k_R Y_1(-2\mathrm{i}k_R r)\int_0^r xM_R(x)J_0(2\mathrm{i}k_R x)\,\mathrm{d}x - 2\mathrm{i}k_R C_5 J_1(2\mathrm{i}k_R r), \tag{E3}$$

and similarly for (4.42),

$$\frac{\mathrm{d}U_I(r)}{\mathrm{d}r} = \pi k_I J_1(2k_I r)\int_0^r xM_I(x)Y_0(2k_I x)\,\mathrm{d}x \\ - \pi k_I Y_1(2k_I r)\int_0^r xM_I(x)J_0(2k_I x)\,\mathrm{d}x - 2k_I C_7 J_1(2k_I r). \tag{E4}$$

Appendix F

The Stokes drift is given by

$$\boldsymbol{v}_{SD} = \frac{2}{\omega}\mathrm{Re}\Big\{\Big[\left(-\mathrm{i}q_f A_1 J_0(q_f r) + kB_1 J_1(q_v r)\right)\left(-q_f^2 A_1 J_0(q_f r) + \frac{1}{r}q_f A_1 J_1(q_f r)\right. \\ \left. + \frac{1}{r}\mathrm{i}kB_1 J_1(q_v r) - \mathrm{i}kq_v B_1 J_0(q_v r)\right)^*\left(\cos^2(k_R z) + \sinh^2(k_I z)\right) \\ + \mathrm{i}\left(-kA_1 J_0(q_f r) + \mathrm{i}q_v B_1 J_0(q_v r)\right)\left(kq_f A_1 J_1(q_f r) + \mathrm{i}k^2 B_1 J_1(q_v r)\right)^* \\ \left(\sin^2(k_R z) + \sinh^2(k_I z)\right)\Big]\boldsymbol{e}_r \\ + \frac{1}{2}\Big[\left(-\mathrm{i}q_f A_1 J_1(q_f r) + kB_1 J_1(q_v r)\right)\left(kq_f A_1 J_1(q_f r) - \mathrm{i}q_v^2 B_1 J_1(q_v r)\right)^* \\ (\sin(2k_R z) - \mathrm{i}\sinh(2k_I z)) \\ + \mathrm{i}\left(-kA_1 J_0(q_f r) + \mathrm{i}q_v B_1 J_0(q_v r)\right)\left(-k^2 A_1 J_0(q_f r) + \mathrm{i}kq_v B_1 J_0(q_v r)\right)^* \\ (\sin(2k_R z) + \mathrm{i}\sinh(2k_I z))\Big]\boldsymbol{e}_z\Big\}. \tag{F1}$$

Appendix G

Schuster & Matz (1940) calculated the streaming velocity outside the viscous boundary layer, for a non-decaying wave along z-axis, as

$$\langle \boldsymbol{v}_2 \rangle^S = -\frac{3}{8}\frac{p_a^2\omega}{c_f^4\rho_0^2} r\cos\left(\frac{2\omega}{c_f}\left(z-\frac{\lambda}{4}\right)\right)\left\{1-\frac{r^2}{a^2}\right\}\boldsymbol{e}_r - \frac{3}{8}\frac{p_a^2}{c_f^3\rho_0^2}\sin\left(\frac{2\omega}{c_f}\left(z-\frac{\lambda}{4}\right)\right)\left\{1-\frac{2r^2}{a^2}\right\}\boldsymbol{e}_z, \tag{G1}$$

where we have shifted the solution along z-axis by $\lambda/4$ to match the position of the velocity node to $z = 0$, as assumed in our formulation.

Schuster & Matz (1940) also assume that $\lambda_R = \lambda$, and the simplified expression for the velocity magnitude at $z = \lambda/8$ and $r = 0$ is given as

$$v_2^{Sz} = \frac{3p_a^2}{8c_f^3\rho_0^2}. \tag{G2}$$

References

Andrade, E.N.D.C. 1931 On the circulations caused by the vibration of air in a tube. *Proc. R. Soc. Lond.* A **134** (824), 445–470.

Andrade, E.N.D.C. 1932 On the groupings and general behaviour of solid particles under the influence of air vibrations in tubes. *Phil. Trans. R. Soc. Lond.* A **230** (681–693), 413–445.

Araz, M.K., Lee, C.-H. & Lal, A. 2003 Ultrasonic separation in microfluidic capillaries. In *IEEE Symposium on Ultrasonics, Honolulu, HI, USA, 5–8 October 2003* (ed. D. E. Yuhas & S. C. Schneider), pp. 1066–1069. IEEE.

Bailliet, H., Gusev, V., Raspet, R. & Hiller, R.A. 2001 Acoustic streaming in closed thermoacoustic devices. *J. Acoust. Soc. Am.* **110** (4), 1808–1821.

Baltean-Carlès, D., Daru, V., Weisman, C., Tabakova, S. & Bailliet, H. 2019 An unexpected balance between outer Rayleigh streaming sources. *J. Fluid Mech.* **867**, 985–1011.

Barnkob, R., Augustsson, P., Laurell, T. & Bruus, H. 2010 Measuring the local pressure amplitude in microchannel acoustophoresis. *Lab on a Chip* **10** (5), 563–570.

Bates, A. 2017 A new resonance tube. *Phys. Teacher* **55** (9), 544–545.

Blackstock, D.T. 2001 *Fundamentals of Physical Acoustics*. ASA.

Boluriaan, S. & Morris, P.J. 2003 Acoustic streaming: from Rayleigh to today. *Intl J. Aeroacoust.* **2** (3), 255–292.

Boyce, W.E., DiPrima, R.C. & Meade, D.B. 2017 *Elementary Differential Equations*. John Wiley & Sons.

Cook, R.V. 1926 Use of pith dust in Kundt's tubes. *Nature* **118** (2961), 157.

Cook, R.V. 1930*a* The formation of striae in a Kundt's tube. *Phys. Rev.* **36** (6), 1098–1199.

Cook, R.V. 1930*b* The formation of striae in a Kundt's tube. *Science* **72** (1869), 422–423.

Cook, R.V. 1931 The formation of striae in a Kundt's tube. *Phys. Rev.* **37** (9), 1189–1190.

Devendran, C., Albrecht, T., Brenker, J., Alan, T. & Neild, A. 2016 The importance of travelling wave components in standing surface acoustic wave (SSAW) systems. *Lab on a Chip* **16** (19), 3756–3766.

Doinikov, A.A., Thibault, P. & Marmottant, P. 2017 Acoustic streaming in a microfluidic channel with a reflector: case of a standing wave generated by two counterpropagating leaky surface waves. *Phys. Rev.* E **96** (1), 013101.

Dvorak, V. 1874 Ueber einige neue Staubfiguren. *Ann. Phys.* **153**, 102–115.

Dvorak, V. 1876 Ueber die akustische Anziehung und Abstossung. *Ann. Phys.* **157**, 42–73.

Eckart, C. 1948 Vortices and streams caused by sound waves. *Phys. Rev.* **73** (1), 68–76.

Goddard, G., Martin, J.C., Graves, S.W. & Kaduchak, G. 2006 Ultrasonic particle-concentration for sheathless focusing of particles for analysis in a flow cytometer. *Cytometry* A **69** (2), 66–74.

Gralinski, I., Raymond, S., Alan, T. & Neild, A. 2014 Continuous flow ultrasonic particle trapping in a glass capillary. *J. Appl. Phys.* **115** (5), 054505.

Hamilton, M.F. & Blackstock, D.T. 1998 *Nonlinear Acoustics*. Academic Press.

HAMILTON, M.F., ILINSKII, Y.A. & ZABOLOTSKAYA, E.A. 2003*a* Acoustic streaming generated by standing waves in two-dimensional channels of arbitrary width. *J. Acoust. Soc. Am.* **113** (1), 153–160.

HAMILTON, M.F., ILINSKII, Y.A. & ZABOLOTSKAYA, E.A. 2003*b* Thermal effects on acoustic streaming in standing waves. *J. Acoust. Soc. Am.* **114** (6), 3092–3101.

HIRAI, N. & EYRING, H. 1958 Bulk viscosity of liquids. *J. Appl. Phys.* **29** (5), 810–816.

HUTCHISSON, E. & MORGAN, F.B. 1931 An experimental study of Kundt's tube dust figures. *Phys. Rev.* **37** (9), 1155–1163.

IMANI, R.J. & ROBERT, E. 2015 Acoustic separation of submicron solid particles in air. *Ultrasonics* **63**, 135–140.

IRONS, E.J. 1929*a* LXI. Studies in the formation of Kundt's tube dust figures—parts I and II. *Lond. Edinburgh Dublin Phil. Mag. J. Sci.* **7** (43), 523–537.

IRONS, E.J. 1929*b* New phenomena in a sounding dust tube. *Nature* **124** (3137), 914.

JAAFAR, R., AYOP, S.K., ISMAIL@ ILLIAS, A.T., HON, K.K., DAUD, A.N.M. & HASHIM, M.H. 2016 Visualization of harmonic series in resonance tubes using a smartphone. *Phys. Teacher* **54** (9), 545–547.

KARLSEN, J.T. & BRUUS, H. 2015 Forces acting on a small particle in an acoustical field in a thermoviscous fluid. *Phys. Rev.* E **92** (4), 043010.

KUNDT, A. 1866 Ueber eine neue Art akustischer Staubfiguren und über die Anwendung derselben zur Bestimmung der Schallgeschwindigkeit in festen Körpern und Gasen. *Ann. Phys.* **203** (4), 497–523.

LIGHTHILL, J. 1978 Acoustic streaming. *J. Sound Vib.* **61** (3), 391–418.

MENGUY, L. & GILBERT, J. 2000 Non-linear acoustic streaming accompanying a plane stationary wave in a guide. *Acta Acust. United with Acust.* **86** (2), 249–259.

MINER, C.S. & DALTON, N.N. 1953 *Glycerol*. Reinhold Publishing Corporation.

NYBORG, W.L. 1953 Acoustic streaming due to attenuated plane waves. *J. Acoust. Soc. Am.* **25** (1), 68–75.

NYBORG, W.L.M. 1965 Acoustic streaming. In *Physical Acoustics* (ed. W. P. Mason), vol. 2, pp. 265–331. Elsevier.

PAPACOSTA, P. & LINSCHEID, N. 2016 An inexpensive and versatile version of Kundt's tube for measuring the speed of sound in air. *Phys. Teacher* **54** (1), 50–51.

QI, Q., JOHNSON, R.E. & HARRIS, J.G. 1995 Boundary layer attenuation and acoustic streaming accompanying plane-wave propagation in a tube. *J. Acoust. Soc. Am.* **97** (3), 1499–1509.

RAYLEIGH, LORD 1884 On the circulation of air observed in Kundt's tubes, and on some allied acoustical problems. *Phil. Trans. R. Soc. Lond.* **175**, 1–21.

SCHLICHTING, H. 1932 Berechnung ebener periodischer Grenzschichtstromungen. *Phys. Z.* **33**, 327–335.

SCHUSTER, K. & MATZ, W. 1940 Über stationäre Strömungen im Kundtschen Rohr. *Akust. Z.* **5**, 349–352.

SNEDDON, I.N. 1946 III. Finite Hankel transforms. *Lond. Edinburgh Dublin Phil. Mag. J. Sci.* **37** (264), 17–25.

SNEDDON, I.N. 1972 *The Use of Integral Transforms*. McGraw-Hill.

SOBANSKI, M.A., TUCKER, C.R., THOMAS, N.E. & COAKLEY, W.T. 2000 Sub-micron particle manipulation in an ultrasonic standing wave: applications in detection of clinically important biomolecules. *Bioseparation* **9** (6), 351–357.

WESTERVELT, P.J. 1953 The theory of steady rotational flow generated by a sound field. *J. Acoust. Soc. Am.* **25** (1), 60–67.

WIKLUND, M., GREEN, R. & OHLIN, M. 2012 Acoustofluidics 14: applications of acoustic streaming in microfluidic devices. *Lab on a Chip* **12** (14), 2438–2451.

WIKLUND, M., NILSSON, S. & HERTZ, H.M. 2001 Ultrasonic trapping in capillaries for trace-amount biomedical analysis. *J. Appl. Phys.* **90** (1), 421–426.

WOLFRAM RESEARCH, INC. 2019 Mathematica, Version 12.0. Champaign, IL, 2019.